Monthly Notices of the ROYAL ASTRONOMICAL SOCIETY

MNRAS **530,** 1866–1884 (2024) https://doi.org/10.1093/mnras/stae959
Advance Access publication 2024 April 9

Particle-in-cell simulations of the magnetorotational instability in stratified shearing boxes

Astor Sandoval,[1]★ Mario Riquelme,[1] Anatoly Spitkovsky[2] and Fabio Bacchini[3,4]

[1]*Departamento de Física, Facultad de Ciencias Físicas y Matemáticas, Universidad de Chile, Santiago, RM 8370449, Chile*
[2]*Department of Astrophysical Sciences, Princeton University, Princeton, NJ 08544, USA*
[3]*Centre for Mathematical Plasma Astrophysics, Department of Mathematics, KU Leuven, Celestijnenlaan 200B, B-3001 Leuven, Belgium*
[4]*Royal Belgian Institute for Space Aeronomy, Solar-Terrestrial Centre of Excellence, Ringlaan 3, B-1180 Uccle, Belgium*

Accepted 2024 April 4. Received 2024 April 4; in original form 2023 August 24

ABSTRACT

The magnetorotational instability (MRI) plays a crucial role in regulating the accretion efficiency in astrophysical accretion discs. In low-luminosity discs around black holes, such as Sgr A∗ and M87, Coulomb collisions are infrequent, making the MRI physics effectively collisionless. The collisionless MRI gives rise to kinetic plasma effects that can potentially affect its dynamic and thermodynamic properties. We present 2D and 3D particle-in-cell (PIC) plasma simulations of the collisionless MRI in stratified discs using shearing boxes with net vertical field. We use pair plasmas, with initial $\beta = 100$ and concentrate on subrelativistic plasma temperatures ($k_{\rm B}T \lesssim mc^2$). Our 2D and 3D runs show disc expansion, particle and magnetic field outflows, and a dynamo-like process. They also produce magnetic pressure dominated discs with (Maxwell stress dominated) viscosity parameter $\alpha \sim 0.5$–1. By the end of the simulations, the dynamo-like magnetic field tends to dominate the magnetic energy and the viscosity in the discs. Our 2D and 3D runs produce fairly similar results, and are also consistent with previous 3D MHD (magnetohydrodynamic) simulations. Our simulations also show non-thermal particle acceleration, approximately characterized by power-law tails with temperature-dependent spectral indices $-p$. For temperatures $k_{\rm B}T \sim 0.05 - 0.3\,mc^2$, we find $p \approx$ 2.2–1.9. The maximum accelerated particle energy depends on the scale separation between MHD and Larmor-scale plasma phenomena in a way consistent with previous PIC results of magnetic reconnection-driven acceleration. Our study constitutes a first step towards modelling from first principles potentially observable stratified MRI effects in low-luminosity accretion discs around black holes.

Key words: acceleration of particles – accretion, accretion discs – dynamo – instabilities – plasmas.

1 INTRODUCTION

The primary driver of accretion in astrophysical discs is believed to be the turbulence generated by the magnetorotational instability (MRI; Balbus & Hawley 1991, 1998), which provides the needed outward transport of angular momentum. Most of our knowledge about the non-linear evolution of the MRI in different disc regimes comes from magnetohydrodynamic (MHD) simulations. However, in the regime where the plasma accretion rate is much lower than the Eddington rate, the Coulomb mean free path of the particles can be much larger than the system size, rendering the disc effectively collisionless and making the MHD approach inapplicable. This collisionless accretion regime is expected, for instance, in the low–hard state of X-ray binaries (Esin, McClintock & Narayan 1997) as well as around the central supermassive black holes of most nearby galaxies, including M87 and Sagittarius A∗ (Sgr A∗) in our own Milky Way (Yuan & Narayan 2014).

The collisionless version of the MRI can give rise to several kinetic plasma phenomena, which may in turn affect its dynamics as well as the thermodynamic properties of the accreting plasma. These kinetic phenomena have been studied mainly via unstratified shearing-box MRI simulations, using either a fluid approach through kinetic-MHD models (Sharma et al. 2006, 2007) or particle simulations that employ either the hybrid or the particle-in-cell (PIC) methods (Riquelme et al. 2012; Hoshino 2013, 2015; Kunz et al. 2016; Inchingolo et al. 2018; Bacchini et al. 2022). One of the relevant kinetic phenomena is the appearance of an anisotropic stress, which is due to the presence of a pressure anisotropy in the accreting turbulence. Previous unstratified shearing-box simulation studies, both based on fluid and particle methods, have found that this anisotropic stress may contribute significantly to the disc viscosity, making the collisionless MRI turbulence more efficient in transporting angular momentum compared to its collisional counterpart.

Another potentially important collisionless phenomenon is the possibly different ion and electron heating rates (e.g. Sharma et al. 2007). However, to date PIC studies have only used an ion to electron mass ratio $m_i/m_e = 1$ (or close to unity), therefore not capturing the possibly different heating efficiencies of the different species. Plasma energization can also include non-thermal particle acceleration. Studying this phenomenon requires fully kinetic treatments of at

★ E-mail: astor.sandoval@ug.uchile.cl

least one species, which has been done through PIC and hybrid simulations. Different levels of non-thermal particle acceleration have indeed been found by these types of studies (Riquelme et al. 2012; Hoshino 2013, 2015; Kunz et al. 2016; Inchingolo et al. 2018; Bacchini et al. 2022), although the conditions under which this acceleration is most efficient and the mechanism(s) underlying this phenomenon remain to be clarified.

An important physical ingredient, so far not included in hybrid or fully kinetic PIC studies of the MRI, is the vertical stratification of the discs. While the unstratified local shearing-box approximation allows us to investigate a disc by focusing on a small vertical section, this approach does not account for potentially important processes in stratified discs, such as outflows, disc expansion, and the generation of a corona, among others. Stratified discs have been included in previous MHD shearing-box simulations of the MRI, which have found that stratification can give rise to important phenomena like outflows and dynamo-like processes, which may in turn affect the overall accretion efficiency of the discs (Bai & Stone 2013; Salvesen et al. 2016). Also, a kinetic-MHD study that considers a stratified disc (Hirabayashi & Hoshino 2017) has found that disc stratification may decrease the importance of anisotropic stress significantly compared to unstratified kinetic-MHD results.

To address these possible effects, our study employs 2D and 3D stratified shearing-box PIC simulations to examine the development of the collisionless MRI. We use equal ion and electron masses, $m_i = m_e = m$ for computational convenience, and focus on the subrelativistic temperature regime, relevant for the inner regions of black hole accretion discs ($k_\mathrm{B}T \lesssim mc^2$, where k_B is the Boltzmann constant, T is the plasma temperature, and c is the speed of light).[1] By comparing with unstratified PIC runs, we show the importance of including stratification to describe phenomena like plasma beta evolution, effective viscosity and particle acceleration. In our 2D runs, we pay special attention to the role played by the ratio between the initial cyclotron frequency of the particles and the Keplerian frequency of the disc, $\omega_{c,0}/\Omega_0$ (hereafter, the scale-separation ratio). In realistic discs, this ratio satisfies $\omega_{c,0}/\Omega_0 \gg 1$ and determines the scale separation between mesoscale MHD phenomena and kinetic microphysical processes. Even though most of our analysis is done in 2D, in this paper we take a step forward by conducting the first fully kinetic 3D simulation of the stratified MRI evolution. This preliminary 3D simulation enables us to compare it with our established 2D results and gain valuable insight into the limitations of the 2D approach. This exploration sets the stage for future investigations aimed at fully unravelling the complexities of the 3D scenario.

The paper is organized as follows. In Section 2, we describe our numerical method and simulation setup. In Sections 3 and 4, we present the general properties of the stratified MRI turbulence in 2D and 3D, respectively. In Section 5, we quantify the effective viscosity in our runs. In Section 6, we analyse the ability of the stratified MRI turbulence to accelerate particles, and in Section 7, we validated the assumptions we made based on the results of our simulations. Finally, we present our conclusions in Section 8.

[1]This choice for the mass ratio is intended to provide a reasonable approximation for the evolution of the ions, which carry most of the inertia of the plasma. For correctly describing the electron dynamics, we would have to reduce the electron mass to realistic values, while keeping the same ion mass. This would require resolving the evolution of the system on much smaller scales, which we plan to pursue in future works.

2 SIMULATION SETUP

We use the electromagnetic PIC code TRISTAN-MP (Buneman 1993; Spitkovsky 2005) in 2D and 3D. Our simulations are performed in the local, shearing-box approximation (Hawley, Gammie & Balbus 1995), using Cartesian coordinates where the x-, y-, and z-axes correspond to the radial, azimuthal (or toroidal), and vertical directions of the disc, respectively. This reference frame rotates with an angular velocity $\boldsymbol{\Omega}_0 = \Omega_0\hat{z}$, corresponding to the Keplerian angular velocity at a radius that coincides with the centre of our simulation box. In order to model a stratified disc, we include the vertical component of the gravitational force produced by the central object, $-m\Omega_0^2 z\hat{z}$, and we initially set up an isothermal disc in hydrostatic equilibrium with a z-dependent density profile:

$$n(z) = n_0 \exp\left(-\frac{z^2}{H_0^2}\right), \tag{1}$$

where n_0 is the plasma density at the disc mid-plane (considering both species), H_0 is the scale height of the disc given by $H_0 = (2k_\mathrm{B}T_0/m)^{1/2}/\Omega_0$, and T_0 is the initial plasma temperature, which is given by $k_\mathrm{B}T_0/mc^2 = 5 \times 10^{-3}$ in all of our runs. Our runs do not include any type of radiative cooling, so a gradual increase in the temperature and scale height of the simulated discs is expected due to dissipation of magnetic energy. This approximation is only valid in extremely low-luminosity accreting systems, which may be the case of Sgr A∗ (Yoon et al. 2020). The whole simulation domain is initially threaded by a vertical, homogeneous magnetic field $\boldsymbol{B}_0 = B_0\hat{z}$, so that the initial plasma β parameter in the disc mid-plane, β_0 ($= 8\pi n_0 k_\mathrm{B}T_0/B_0^2$), has a value of $\beta_0 = 100$. These choices for T_0 and β_0 imply that the initial Alfvén velocity in the disc mid-plane, $v_{A,0}$ ($=B_0/(4\pi n_0 m)^{1/2}$), is $v_{A,0}/c = 10^{-2}$ in all of our runs.

2.1 Basic equations

In our rotating frame, the time derivative of particles momentum $\boldsymbol{p} = (p_x, p_y, p_z)$ is determined by the Lorentz force, the radial and vertical components of gravity, and the Coriolis force:[2]

$$\frac{\mathrm{d}\boldsymbol{p}}{\mathrm{d}t} = q\left(\boldsymbol{E} + \frac{\boldsymbol{v}}{c}\times\boldsymbol{B}\right) + 3m\Omega_0^2 x\hat{\boldsymbol{x}} - m\Omega_0^2 z\hat{\boldsymbol{z}} - 2\boldsymbol{\Omega}_0\times\boldsymbol{p}, \tag{2}$$

where $\boldsymbol{v} = \boldsymbol{p}/(\gamma m) = (v_x, v_y, v_z)$, q, $\boldsymbol{E}$ and $\boldsymbol{B}$ are, respectively, the particle velocity, the particle charge, and the electric and magnetic fields. In this non-inertial frame, Maxwell's equations also acquire extra terms, which modify the evolution of the electric field as (Schiff 1939):

$$\frac{\partial\boldsymbol{E}}{\partial t} = c\nabla\times\boldsymbol{B} - 4\pi\boldsymbol{J} + \frac{\boldsymbol{v}_0}{c}\times\frac{\partial\boldsymbol{B}}{\partial t} - \nabla\times\left(\boldsymbol{v}_0\times\left(\boldsymbol{E} - \frac{\boldsymbol{v}_0}{c}\times\boldsymbol{B}\right)\right), \tag{3}$$

where $\boldsymbol{J}$ is the current density and $\boldsymbol{v}_0$ is the Keplerian rotation velocity of the disc at the centre of our simulation box (the evolution of the magnetic field $\partial\boldsymbol{B}/\partial t = -c\nabla\times\boldsymbol{E}$ is not modified in the rotating frame). As discussed in Riquelme et al. (2012), the terms proportional to $\boldsymbol{v}_0$ in equation (3) can in principle be comparable to the displacement current $\partial\boldsymbol{E}/\partial t$, but should not change the non-relativistic MHD behaviour of the plasma. This is because, in the non-relativistic regime ($|\boldsymbol{v}_0| = v_0 \ll c$), these extra terms are always

[2]Since Coriolis forces conserve kinetic energy, the standard Coriolis expression for the evolution of $\boldsymbol{v}$, $\mathrm{d}\boldsymbol{v}/\mathrm{d}t = 2\boldsymbol{\Omega}_0\times\boldsymbol{v}$, can be directly translated into a relativistic momentum $\boldsymbol{p}$ evolution as $\mathrm{d}\boldsymbol{p}/\mathrm{d}t = 2\boldsymbol{\Omega}_0\times\boldsymbol{p}$.

much smaller than the first term on the right-hand side of equation (3) ($c\nabla \times \boldsymbol{B}/4\pi$). Therefore, the current density $\boldsymbol{J}$ should still adjust to satisfy $\boldsymbol{J} \approx c\nabla \times \boldsymbol{B}/4\pi$, as assumed in the non-relativistic MHD approach. Thus, as it has been done in all previous PIC and hybrid studies of the MRI, we drop the terms proportional to v_0 in equation (3) and solve the conventional Maxwell's equations. We are thus implicitly assuming that these (beyond MHD) modifications to the displacement current do not affect considerably the kinetic MRI dynamics.

2.2 Shearing coordinates

Simulating the MRI in the shearing-box approximation requires implementing shearing periodic boundary conditions in the radial (x) direction (e.g. Hawley et al. 1995). We do this by employing *shearing coordinates* (Riquelme et al. 2012), in which the grid follows the shearing velocity profile within the shearing box, allowing the use of standard periodic boundary conditions in the radial (x) direction. However, the use of shearing coordinates introduces modifications in the evolution of the electric and magnetic fields, as well as in the evolution of particles momenta and positions. These modifications are described in detail in the appendix of Riquelme et al. (2012) and, for easy access, are also summarized below.

In the shearing coordinates, the fields evolve as

$$\frac{\partial \boldsymbol{B}}{\partial t} = -c\nabla \times \boldsymbol{E} - \frac{3\Omega_0}{2} B_x \hat{\boldsymbol{y}} + \frac{3\Omega_0}{2}\left(ct\frac{\partial \boldsymbol{E}}{\partial y} + \frac{y}{c}\frac{\partial \boldsymbol{E}}{\partial t}\right) \times \hat{\boldsymbol{x}} \text{ and} \tag{4}$$

$$\frac{\partial \boldsymbol{E}}{\partial t} = c\nabla \times \boldsymbol{B} - 4\pi \boldsymbol{J} - \frac{3\Omega_0}{2} E_x \hat{\boldsymbol{y}} - \frac{3\Omega_0}{2}\left(ct\frac{\partial \boldsymbol{B}}{\partial y} + \frac{y}{c}\frac{\partial \boldsymbol{B}}{\partial t}\right) \times \hat{\boldsymbol{x}}. \tag{5}$$

The last terms in these equations, which are proportional to y/c (hereafter, the y-dependent terms), can, however, be neglected in the $v_{A,0}/c \ll 1$ regime, as it is shown below. This can be seen considering that the size of our shearing boxes in the y-direction should be typically a few times the wavelength of the most unstable MRI modes $\lambda_{\rm MRI} = 2\pi v_{A,0}/\Omega_0$, which means that $\Omega_0 y \sim v_{A,0}$ (the fact that $\lambda_{\rm MRI}$ is the dominant scale of the MRI turbulence even in its non-linear stage will be shown in Section 4.1 and further discussed in Section 7). Also, assuming that the order of magnitude of the time derivative of any field component f should satisfy $\partial f/\partial t \sim \Omega_0 f$, one can calculate the ratios between the magnitudes of the y -dependent terms in equations (4) and (5) and the left-hand side of these equations, obtaining:

$$\frac{\left|(\Omega_0 y/c)\partial \boldsymbol{E}/\partial t\right|}{\left|\partial \boldsymbol{B}/\partial t\right|} \sim \frac{|\boldsymbol{E}|}{|\boldsymbol{B}|}\frac{v_{A,0}}{c}, \tag{6}$$

for equation (4) and

$$\frac{\left|(\Omega_0 y/c)\partial \boldsymbol{B}/\partial t\right|}{\left|\partial \boldsymbol{E}/\partial t\right|} \sim \frac{|\boldsymbol{B}|}{|\boldsymbol{E}|}\frac{v_{A,0}}{c} \tag{7}$$

for equation (5). Since in general $|\boldsymbol{E}|/|\boldsymbol{B}| \lesssim 1$ (which is verified in Section 7), the right-hand side of equation (6) is much smaller than unity as long as $v_{A,0}/c \ll 1$, implying that the y-dependent term in equation (4) can be safely neglected. The right-hand side of equation (7), on the other hand, is not necessarily $\ll 1$ since its value depends on the precise magnitude of the ratio $|\boldsymbol{E}|/|\boldsymbol{B}|$, which makes the y-dependent term in equation (5) not necessarily negligible. However, using the approximation $\nabla f \sim \lambda_{\rm MRI}^{-1} f \sim (\Omega_0/v_{A,0}) f$, we can calculate the ratio between the magnitude of this y-dependent term and an estimate of the magnitude of the first term on the right-hand side of equation (5) ($c\nabla \times \boldsymbol{B}$), obtaining:

$$\frac{\left|(\Omega_0 y/c)\partial \boldsymbol{B}/\partial t\right|}{\left|c\nabla \times \boldsymbol{B}\right|} \sim \left(\frac{v_{A,0}}{c}\right)^2. \tag{8}$$

This implies that dropping the y-dependent term in equation (5) should not change the non-relativistic MHD behaviour of the plasma, in which $\boldsymbol{J} \approx c\nabla \times \boldsymbol{B}/4\pi$, and is also consistent with our previous choice of ignoring the terms proportional to v_0 in equation (3). Doing a similar analysis, we find that the ratio between the magnitudes of the third and the first terms on the right-hand side of equation (5) is

$$\frac{\Omega_0 |E_x|}{\left|c\nabla \times \boldsymbol{B}\right|} \sim \frac{|\boldsymbol{E}|}{|\boldsymbol{B}|}\frac{v_{A,0}}{c}, \tag{9}$$

so, for consistency, we also neglect the former. Therefore, in our simulations we evolve the fields by solving the equations:

$$\frac{\partial \boldsymbol{B}}{\partial t} = -c\nabla \times \boldsymbol{E} - \frac{3}{2}\Omega_0 B_x \hat{\boldsymbol{y}} + \frac{3}{2}\Omega_0 t\, c\frac{\partial \boldsymbol{E}}{\partial y} \times \hat{\boldsymbol{x}} \text{ and} \tag{10}$$

$$\frac{\partial \boldsymbol{E}}{\partial t} = c\nabla \times \boldsymbol{B} - 4\pi \boldsymbol{J} - \frac{3}{2}\Omega_0 t\, c\frac{\partial \boldsymbol{B}}{\partial y} \times \hat{\boldsymbol{x}}. \tag{11}$$

In terms of particles evolution, in the shearing coordinates each particle's momentum $\boldsymbol{p}$ evolves as (Riquelme et al. 2012):

$$\frac{\mathrm{d}\boldsymbol{p}}{\mathrm{d}t} = 2\Omega_0 p_y \hat{\boldsymbol{x}} - \frac{1}{2}\Omega_0 p_x \hat{\boldsymbol{y}} - m\Omega_0^2 z\hat{\boldsymbol{z}} + q\left(\boldsymbol{E} + \frac{\boldsymbol{v}}{c} \times \boldsymbol{B}\right), \tag{12}$$

which is valid in the limit $\Omega_0 y \sim v_{A,0} \ll c$ and as long as the shear velocity of the plasma within our simulation domain, $\boldsymbol{v}_s$, is non-relativistic. This last assumption is justified since $v_s \sim \Omega_0 x$, and x in our shearing box is also of the order of a few times $\lambda_{\rm MRI} = 2\pi v_{A,0}/\Omega_0$. This implies that $|\boldsymbol{v}_s| \sim \Omega_0 x \sim v_{A,0}$, making equation (12) valid in the regime $v_{A,0} \ll c$.

We emphasize that equations (10)–(12) are valid under the assumption that $\Omega_0 x$, $\Omega_0 y$ are $\ll c$. Since the typical scale of the MRI turbulence along the x- and y-axes is determined by $\lambda_{\rm MRI} = 2\pi v_{A,0}/\Omega_0$ even in the non-linear MRI regime (as checked in Section 4.1 and discussed in Section 7), these equations are valid as long as $v_{A,0} \ll c$, which is reasonably well satisfied by our choice $v_{A,0}/c = 10^{-2}$. Additionally, these equations also require $|\boldsymbol{E}|/|\boldsymbol{B}| \lesssim 1$ and the plasma to be in the non-relativistic MHD regime where $\boldsymbol{J} \approx c\nabla \times \boldsymbol{B}/4\pi$ (which implies the instantaneous Alfvén velocity to satisfy $v_A \ll c$). In Section 7, we check that these assumptions are also satisfied in the disc region of our runs during almost the entire simulation time.

Finally, the evolution of the particles position $\boldsymbol{r} = (x, y, z)$ is given by:

$$\frac{\mathrm{d}\boldsymbol{r}}{\mathrm{d}t} = \boldsymbol{v} + \frac{3}{2}\Omega_0 t\, v_x \hat{\boldsymbol{y}}, \tag{13}$$

which is obtained combining equations (A30) and (A35) of Riquelme et al. (2012) also in the limit in which $\boldsymbol{v}_s$ is non-relativistic.

In order to safeguard the numerical stability and accuracy of our simulations, every time the factor $(3/2)\Omega_0 t$ on the right-hand side of equations (10), (11), and (13) equals an integer, we reset these equations to their initial ($t = 0$) shape. This implies a periodic 'unshearing' of our shearing grid that, therefore, requires

Table 1. Simulations parameters.

Run	UN2D-20	ST2D-28	ST2D-20	ST2D-14	ST2D-10	ST2D-7	ST2D-3.5	ST3D-3.5	ST2D-20LR	ST2D-20HR
$\omega_{c,0}/\Omega_0$	20	28	20	14	10	7	3.5	3.5	20	20
$L_x\ [2\pi v_{A,0}/\Omega_0]$	22	35	43	47	46	46	48	24	44	44
$L_y\ [2\pi v_{A,0}/\Omega_0]$	–	–	–	–	–	–	–	24	–	–
$L_z\ [2\pi v_{A,0}/\Omega_0]$	22	120	89	95	92	93	96	96	90	90
$\Delta\ [c/\omega_{p,0}]$	0.35	0.35	0.35	0.35	0.35	0.35	0.35	0.35	0.5	0.25
$N_{\rm ppc}$	25	400	350	200	200	200	200	30	350	350
$\Delta t\ [\Delta/c]$	0.45	0.45	0.45	0.45	0.45	0.45	0.45	0.225	0.45	0.45

Notes. We list the initial parameters of our simulations, which are: the scale-separation ratio $\omega_{c,0}/\Omega_0$, where $\omega_{c,0} = |q|B_0/mc$ is the initial cyclotron frequency of the particles, the box size along the different axes (L_x, L_y, and L_z) in terms of $\lambda_{\rm MRI} = 2\pi v_{A,0}/\Omega_0$, the grid spacing Δ (equal in all dimensions) in terms of the initial plasma skin depth, $c/\omega_{p,0} = c/(4\pi n_0 q^2/m)^{1/2}$, the initial number $N_{\rm ppc}$ of particles (ions and electrons) per cell, and the simulation time-step Δt in units of Δ/c, where c is the speed of light.

a remapping of the electric and magnetic fields, as well as of the particles positions. This periodic redefinition of the time origin in our runs means that the factors $(3/2)\Omega_0 t$ in equations (10), (11), and (13) never surpass unity. Notice also that the presence of the term proportional to $(3/2)\Omega_0 t$ in equation (13) implies that relativistic particles may in principle change position in the y-direction at a rate close to twice the speed of light. This should not be considered a violation of special relativity, since this equation only describes the update of particle positions in our non-inertial, time-varying shearing coordinates. Also, we have empirically found that the terms proportional to $(3/2)\Omega_0 t$ do not affect the numerical stability and energy conservation properties of our method as long as we use a time-step $\Delta t \lesssim 0.25\Delta/c$, where Δ is the grid spacing (this has also been tested in previous works where this method has been used, as, e.g. in Riquelme, Quataert & Verscharen 2015). Because of this, in our 3D runs we use $\Delta t = 0.225\Delta/c$. In the 2D simulations, where the time-dependent term $(3/2)\Omega_0 t$ is absent from equations (10), (11), and (13), we use the less stringent time-step $\Delta t = 0.45\Delta/c$, which is smaller than required by the Courant–Friedrichs–Lewy condition in 2D (e.g. Sironi & Cerutti 2017).

We emphasize that, in order to obtain our plasma evolution equations, we have assumed a non-relativistic plasma with $v_A/c \ll 1$, which rotates at non-relativistic velocities ($v_0 \ll c$). This implies that our work strictly applies to a plasma at radii significantly larger than the gravitational radius of a central black hole. For this reason, in this work we concentrate on a subrelativistic regime, where the plasma temperature satisfies $k_{\rm B}T \lesssim mc^2$. Notice, however, that the treatment of individual particles is relativistic, since (as we see below) a small fraction of them can still be non-thermally accelerated to energies much larger than mc^2.

2.3 Boundary conditions along z

Using shearing coordinates allows the use of periodic boundary conditions both in the x (radial) and y (toroidal) coordinates. In the z coordinate we use open boundary conditions, which allow the existence of field and particle outflows in our stratified setup. Thus, in our runs particles are removed from the simulation box after they cross the vertical boundaries, while the fields are absorbed by these boundaries. This configuration effectively prevents outflowing fields from rebounding into the simulation domain (Cerutti et al. 2015; Belyaev 2015; Sironi, Giannios & Petropoulou 2016). This is done by implementing an absorption layer of width $\Delta_{\rm abs}$ in the vertical boundaries, where the terms

$$-\eta(z)(\boldsymbol{B}-\boldsymbol{B}_0) \quad \text{and} \quad -\eta(z)\boldsymbol{E} \tag{14}$$

are added to the right-hand side of equations (10) and (11), respectively. We use $\Delta_{\rm abs} = 50$ cells and $\eta(z) = (40/\Delta t)(|z - z_{\rm abs}|/\Delta_{\rm abs})^3$ within the absorption layer ($\eta(z) = 0$ otherwise), where $z_{\rm abs}$ is the inner edge of the absorption layer and Δt is the simulation time-step.

2.4 Numerical parameters

The simulations presented in this paper and their numerical parameters are listed in Table 1, with all physical quantities in stratified runs corresponding to plasma conditions in the disc mid-plane. These parameters are the scale-separation ratio $\omega_{c,0}/\Omega_0$, where $\omega_{c,0} = |q|B_0/mc$ is the initial cyclotron frequency of the particles, the box size along the different axes (L_x, L_y, and L_z) in terms of $\lambda_{\rm MRI}$, the grid spacing Δ in terms of the initial plasma skin depth, $c/\omega_{p,0} = c/(4\pi n_0 q^2/m)^{1/2}$, the initial number $N_{\rm ppc}$ of macroparticles (ions and electrons) per cell and the time-step Δt in terms of Δ/c. Notice that we ran simulations using several values of Δ, $N_{\rm ppc}$ and L_x, L_y, and L_z to make sure that our results are numerically converged. Table 1 includes some simulations with different values of $\Delta\ [c/\omega_{p,0}]$ in order to explicitly show that our spatial resolution is sufficient to capture the relevant MRI physics.

2.5 Notation convention

In this section, we introduce various types of averages denoted by angled brackets with different subscripts, namely $\langle A\rangle_x$, $\langle A\rangle_{x-y}$, and $\langle A\rangle_v$. $\langle A\rangle_x$ denotes the average along the x-axis at a fixed height z for 2D stratified simulations, $\langle A\rangle_{x-y}$ denotes the average over the x–y plane at a fixed z for 3D stratified simulations, and $\langle A\rangle_v$ represents the average taken over the volume of the disc for stratified simulations, while for unstratified simulations it represents the average over the entire simulation domain.

Additionally, we use an overline notation ($\overline{\ }$) for quantities that are computed as the ratio of two volume averages. For instance, for the plasma β and temperature we define $\overline{\beta} \equiv \langle 8\pi P\rangle_v/\langle B^2\rangle_v$ and $k_B\overline{T} \equiv \langle P\rangle_v/\langle n\rangle_v$. In these expressions, $\langle P\rangle_v = \langle P_\parallel\rangle_v/3 + 2\langle P_\perp\rangle_v/3$, where P denotes the isotropic pressure, and $P_\parallel$ and $P_\perp$ correspond to the pressure parallel and perpendicular to the local magnetic field, respectively. Notice that throughout this work, P is calculated within the frame of reference that moves with the bulk plasma velocity (i.e. the frame where the average momentum of the particles within a fluid element cancels out).

Since in the stratified runs these averages are calculated in the disc region, we define this region through the condition $|z| < H(\overline{T})$, where $H(\overline{T}) = (2k_{\rm B}\overline{T}/m)^{1/2}/\Omega_0$ denotes the instantaneous scale height of the disc. Notice that the calculation of $\overline{T}$ has to be done in the disc region itself, whose definition depends on $\overline{T}$ through the

inequality $|z| < H(\overline{T})$, implying that the $\overline{T}$ of the disc has to be determined recursively.

3 2D RESULTS

In this section, we describe the stratified MRI turbulence using 2D simulations, paying special attention to the difference between stratified and unstratified simulations and to the role played by the scale-separation ratio $\omega_{c,0}/\Omega_0$. In Section 3.1, we analyse the properties of the turbulence, and in Section 3.2 we show the evolution of the plasma properties in the disc.

3.1 Turbulence properties in 2D

Fig. 1 shows three snapshots of the squared magnetic fluctuations δB^2 (where $\delta B = |\delta \boldsymbol{B}|$ and $\delta \boldsymbol{B} = \boldsymbol{B} - \boldsymbol{B}_0$) and of the particle density n for the stratified 2D run ST2D-20 ($\omega_{c,0}/\Omega_0 = 20$). Panels (a) and (b) show the initial formation of non-linear channel flows at time $t = 2.5$ $[2\pi/\Omega_0]$. These channel flows appear both in δB^2 and n and are more clearly formed within the disc region ($|z| < H(\overline{T})$), which is marked by the horizontal dotted lines in all the panels. Panels (c) and (d) show the same quantities but at $t = 3.25$ $[2\pi/\Omega_0]$, when the channel flows have already experienced reconnection, breaking into a turbulent state. At that moment, the disc thickness has increased due to plasma heating and significant particle and magnetic field outflows occur. This turbulent state continues during the entire simulation and is accompanied by a permanent puffing up of the disc, as shown by panels (e) and (f), corresponding to $t = 4.5$ $[2\pi/\Omega_0]$.

Our 2D runs also show the formation of a large scale, preferentially toroidal dynamo-like field, similar to those observed in previous MHD studies (e.g. Bai & Stone 2013; Salvesen et al. 2016). This is seen in panel (a) of Fig. 2, which shows $\langle B_y \rangle_x$ as a function of time t and of the vertical coordinate z. We see that a net $\langle B_y \rangle_x$ is formed, with a maximum amplitude of ∼30–40 B_0 during the non-linear stage of the stratified simulation and with oposite signs inside and outside the disc. The amplitude of $\langle B_y \rangle_x$ is very close to the one observed by previous equivalent 3D MHD simulations of the stratified MRI with initial $\beta_0 = 100$ in the disc mid-plane (Salvesen et al. 2016).

In order to explore the effect of the scale-separation ratio $\omega_{c,0}/\Omega_0$ on the 2D turbulence structure, Fig. 3 shows δB^2 and n in the non-linear MRI state ($t = 4$ $[2\pi/\Omega_0]$) for an analogous run using $\omega_{c,0}/\Omega_0 = 3.5$ (run ST2D-3.5) instead of $\omega_{c,0}/\Omega_0 = 20$. By comparing with panels (e) and (f) of Fig. 1, we see that the scale-separation ratio does not appear to produce a qualitative change in the properties of the 2D MRI turbulence, preserving features such as disc thickness increase and the presence of outflows. Run ST2D-3.5 also shows significant dynamo-like activity, as seen in panel (b) of Fig. 2, where a net $\langle B_y \rangle_x$ field appears similarly to the case of run ST2D-20 in panel (a).

The weak effect of $\omega_{c,0}/\Omega_0$ on the field structure of the stratified MRI can also be seen in the magnetic field power spectra, which are shown in Fig. 4 for runs with $\omega_{c,0}/\Omega_0 = 7$, 10, 14, 20, and 28 (all of them at $t \approx 5$ $[2\pi/\Omega_0]$). Panel (a) shows the spectra of the poloidal component of the magnetic field, $\mathrm{d}(|\tilde{B}_x(k)|^2 + |\tilde{B}_z(k)|^2)/\mathrm{dln}(k)$ ($\tilde{B}_x(k)$ and $\tilde{B}_z(k)$ are the Fourier transform of the x and z components of $\boldsymbol{B}$ and k is the corresponding wavenumber), while panel (b) shows the spectra of the toroidal component, $\mathrm{d}|\tilde{B}_y(k)|^2/\mathrm{dln}(k)$. For all the values of $\omega_{c,0}/\Omega_0$, the spectra show similar shapes, with a break at $k\rho_l \sim 1$ ($k\rho_l = 1$ is marked by the coloured dots on each line), where ρ_l is the typical particle Larmor

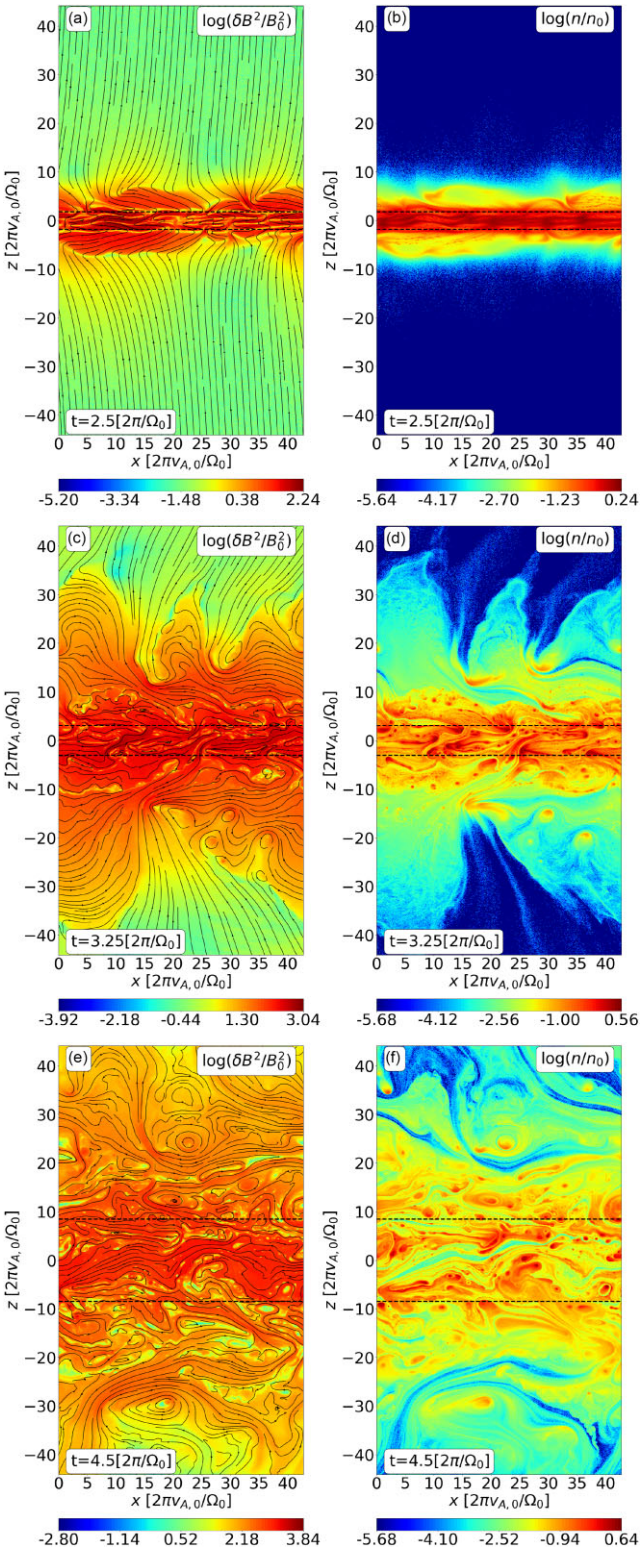

Figure 1. Squared magnetic fluctuations δB^2 (left) and plasma density n (right) for simulation ST2D-20 at $t = 2.5$, 3.25, and 4.5 $[2\pi/\Omega_0]$. The black arrows in the left panels show the total magnetic field direction. The horizontal dotted lines in all the panels mark the region defined as disc region in our analysis (i.e. $|z| < H(\overline{T})$).

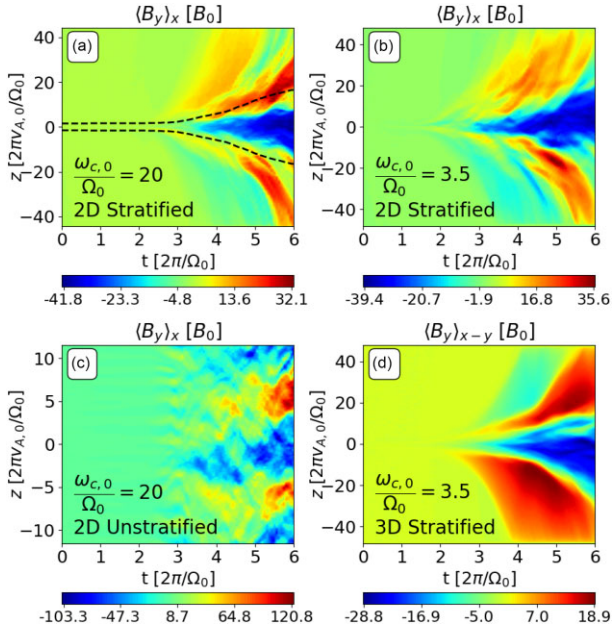

Figure 2. Panels (a)–(c) show the toroidal magnetic component B_y averaged over the x-axis, $\langle B_y \rangle_x$, as a function of the time t and the vertical coordinate z for the 2D runs ST2D-20, ST2D-3.5, and UN2D-20, respectively. The black dashed line in panel (a) marks the disc region ($|z| < H(\overline{T})$). Similarly, panel (d) shows B_y averaged over the x–y plane for the 3D run ST3D-3.5.

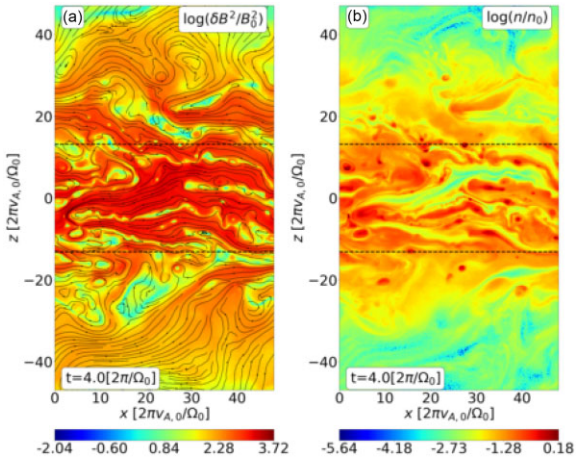

Figure 3. Panels (a) and (b) are analogous to panels (e) and (f) of Fig. 1, but for a run using a much smaller scale-separation ratio $\omega_{c,0}/\Omega_0 = 3.5$ (run ST2D-3.5).

radius, defined as $\rho_l \equiv mc(3k_B\overline{T}/m)^{1/2}/|q|\langle B^2\rangle_v^{1/2}$. Their main difference is the location of the break of the spectra, which moves to larger wavenumbers (in units of $\lambda_{MRI}^{-1} = \Omega_0/2\pi v_{A,0}$) as $\omega_{c,0}/\Omega_0$ increases, implying a growing separation between the kinetic (ρ_l) and the MHD (λ_{MRI}) scales.[3] However, apart from this growing separation between scales, increasing $\omega_{c,0}/\Omega_0$ does not significantly affect the qualitative shape of the power spectra.

[3]Notice that, as explained in Section 2.5, $\overline{T}$ is calculated in the frame of each fluid element, so ρ_l does not include the bulk motion of the plasma.

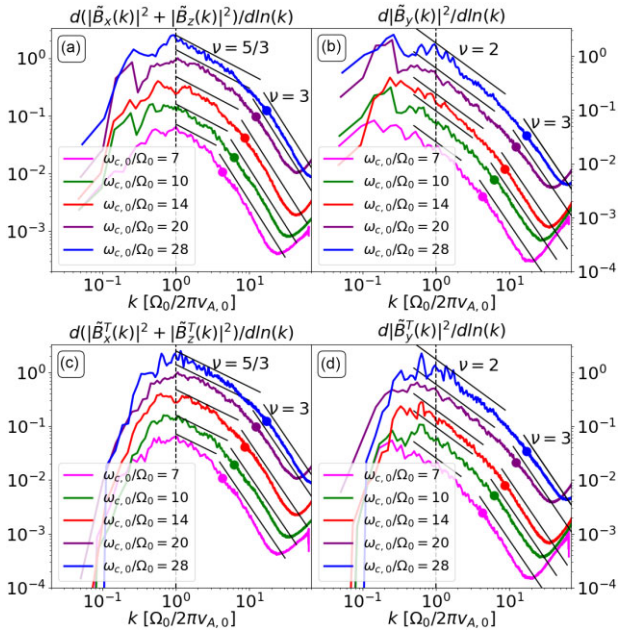

Figure 4. Panels (a) and (b) show the power spectra of the poloidal and toroidal components of the total magnetic field, $d(|\tilde{B}_x(k)|^2 + |\tilde{B}_z(k)|^2)/dln(k)$ and $d|\tilde{B}_y(k)|^2/dln(k)$, for 2D stratified runs with $\omega_{c,0}/\Omega_0 = 7$, 10, 14, 20, and 28. Panels (c) and (d) are analogous to panels (a) and (b), but considering only the turbulent component of the magnetic field, $\mathbf{B}^T$. In all the panels, the spectra use arbitrary normalization and the wavenumber k is normalized by $\Omega_0/2\pi v_{A,0}$.

Panels (a) and (b) also compare $d(|\tilde{B}_x(k)|^2 + |\tilde{B}_z(k)|^2)/dk$ and $d|\tilde{B}_y(k)|^2/dk$ with power-law functions of index ν ($\propto k^{-\nu}$) and show that, at sub-Larmor scales ($k\rho_l \gtrsim 1$), the poloidal and toroidal spectra are approximately consistent with $\nu \approx 3$. This $\nu \approx 3$ behaviour is expected for kinetic Alfvén wave turbulence (e.g. Passot & Sulem 2015) and it has also been observed in previous unstratified 2D and 3D kinetic simulations (Kunz et al. 2016; Inchingolo et al. 2018; Bacchini et al. 2022). Above Larmor scales ($k\rho_l < 1$) the poloidal spectra show a peak at $k\,2\pi v_{A,0}/\Omega_0 \sim 1$, followed by a power-law region characterized by $\nu \approx 5/3$. The toroidal spectra, on the other hand, has a peak at $k\,2\pi v_{A,0}/\Omega_0 \sim 0.2$, followed first by an approximately flat region for $0.2 \lesssim k\,2\pi v_{A,0}/\Omega_0 \lesssim 1$ and then by a steeper $\nu \approx 2$ region for $k\,2\pi v_{A,0}/\Omega_0 \gtrsim 1$. The nearly flat behaviour of the toroidal spectra at $0.2 \lesssim k\,2\pi v_{A,0}/\Omega_0 \lesssim 1$ is significantly affected by the presence of the dynamo-like field. Indeed, panels (c) and (d) of Fig. 4 show the poloidal and toroidal spectra of the 'turbulent' part of the magnetic field, $\mathbf{B}^T$, which is obtained by removing the contribution from the dynamo-like field:

$$\mathbf{B}^T \equiv \mathbf{B} - \mathbf{B}^D, \tag{15}$$

where $\mathbf{B}^D \equiv \langle \mathbf{B} \rangle_x$. While the turbulent and total spectra of the poloidal field are very similar [see panels (a) and (c), respectively], the turbulent spectra of the toroidal field (panel d) decrease substantially at $0.2 \lesssim k\,2\pi v_{A,0}/\Omega_0 \lesssim 1$ compared to the total toroidal spectra (panel b), maintaining its $\nu \approx 2$ behaviour for $k\,2\pi v_{A,0}/\Omega_0 \gtrsim 1$. The $\nu \approx 5/3$ and 2 behaviours of the poloidal and toroidal components of the turbulent field is similar to the unstratified results from 3D MHD simulations of the MRI (e.g. Walker, Lesur & Boldyrev 2016), as well as the ones of 3D kinetic simulations (Kunz et al. 2016; Bacchini et al. 2022). We show in Appendix A that these results are not affected by the spatial resolution of our simulations.

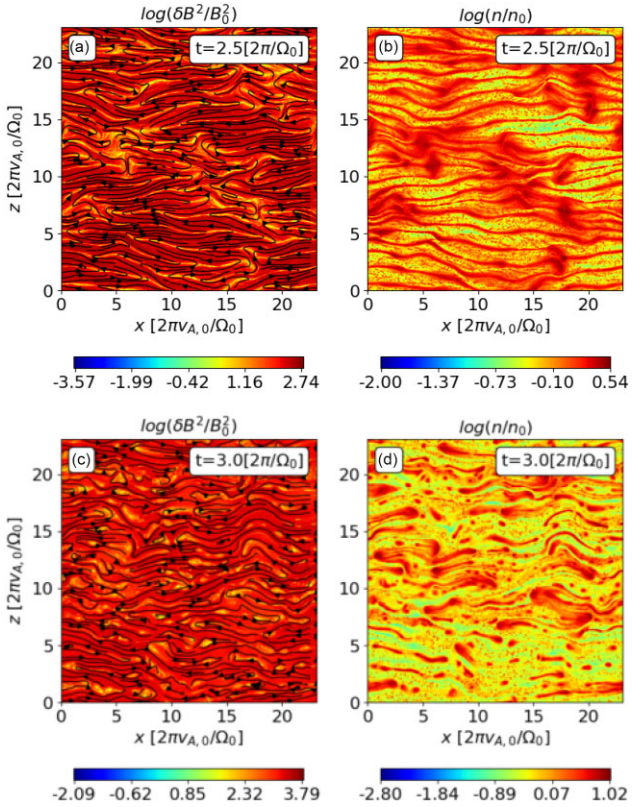

Figure 5. The squared magnetic fluctuations δB^2 (left) and the plasma density n (right) for simulation UN2D-20 at $t = 2.5$ and 3 $[2\pi/\Omega_0]$. The black arrows in the δB^2 panels show the total magnetic field projected on the x–z plane.

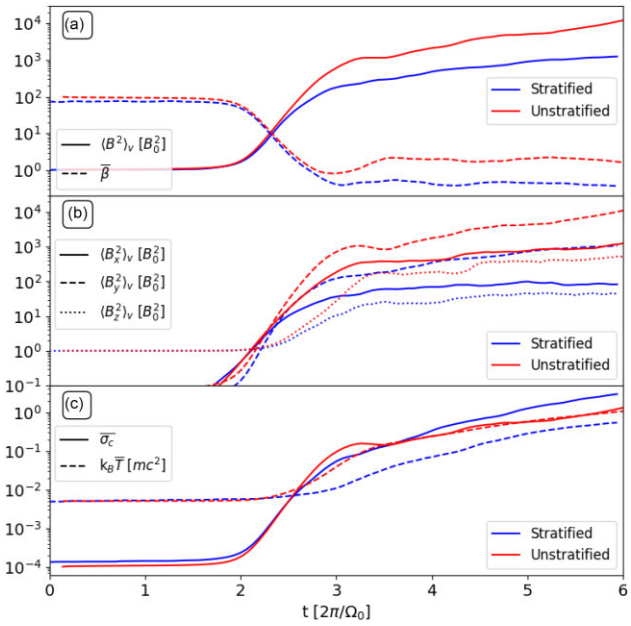

Figure 6. Plasma properties as a function of time t for the disc region of the stratified run ST2D-20 and for the entire domain of the unstratified run UN2D-20, respectively. Panel (a) shows $\langle B^2\rangle_v$ (solid) and $\overline{\beta}$ (dashed). Panel (b) shows the contributions to $\langle B^2\rangle_v$ by the x (solid), y (dashed), and z (dotted) components of the magnetic field. Panel (c) shows $\overline{\sigma}_c$ (solid) and $\overline{T}$ (dashed).

3.2 Disc properties in 2D

In this section, we show the evolution of the average disc properties in our 2D runs, paying attention to the way these properties are affected by the presence of stratification and by the scale-separation ratio $\omega_{c,0}/\Omega_0$.

In order to assess the effect of stratification, we compare run ST2D-20 with the analogous unstratified run UN2D-20, with the same initial conditions as in the disc mid-plane of run ST2D-20. Fig. 5 shows δB^2 and n for run UN2D-20 at the moment when non-linear channel flows appear ($t = 2.5$ $[2\pi/\Omega_0]$) and then when these channel flows have reconnected and broken into turbulence ($t = 3$ $[2\pi/\Omega_0]$). At first glance, this figure suggests that the evolution of the MRI turbulence in run UN2D-20 is similar to the one in the disc region of run ST2D-20. However, the average plasma properties between these two runs differ substantially, as shown in Fig. 6. Panel (a) of Fig. 6 shows the evolution of $\langle B^2\rangle_v$ in the disc of run ST2D-20 (solid blue line) and in the whole volume of the analogous unstratified run UN2D-20 (solid red line). In both simulations there is an initial exponential growth regime that transitions to a much slower growth regime at $t \approx 3$ $[2\pi/\Omega_0]$. Also, the two runs show the lack of a complete magnetic field saturation. However, at $t \gtrsim 3$ $[2\pi/\Omega_0]$, at any given time the unstratified case reaches a $\langle B^2\rangle_v$ magnitude ∼5–10 times larger than in the stratified case. This factor ∼5–10 larger amplification applies similarly to the three components of the magnetic field, as can be seen from panel (b) of Fig. 6.

Interestingly, the B_y component in the unstratified case appears to be dominated by a large scale, dynamo-like component, similarly to what occurs in the stratified runs. This can be seen from panel (c) of Fig. 2, which shows $\langle B_y\rangle_x$ for run UN2D-20. We see that by $t = 6$ $[2\pi/\Omega_0]$, $\langle B_y\rangle_x$ reaches an amplitude ∼$100B_0$, similar to the one of the total B_y component, as shown by the dashed red line in panel (b) of Fig. 6. However, whereas the dynamo activity in the analogous stratified run ST2D-20 (shown in panel a of Fig. 2) produces a rather homogeneous $\langle B_y\rangle_x$ in the disc region ($|z| < H(\overline{T})$, marked by the dashed black lines), the characteristic wavelength of the large-scale B_y field in the unstratified case is ∼4 times smaller. We thus interprete the large-scale B_y field in the unstratified case as a growth in the wavelength of the MRI modes, being therefore of different nature compared to the larger scale $\langle B_y\rangle_x$ of the stratified runs.

The time when the stratified simulation significantly slows down its growth ($t \approx 3$ $[2\pi/\Omega_0]$) coincides with the moment when stratification effects, such as outflows and disc expansion become important, as can be seen from Fig. 1. Notice that this moment coincides with the time when the disc temperature starts increasing significantly, as we can see from the dashed-blue line in panel (c) of Fig. 6, showing a connection between energy dissipation and disc expansion and outflow generation.

Despite the fact that the magnetic field is amplified less in the stratified case, the average cold sigma parameter $\overline{\sigma}_c$ ($\equiv \langle B^2\rangle_v/\langle 4\pi nmc^2\rangle_v$) is larger in the non-linear regime of these runs. This is shown by the solid blue and solid red lines in panel (c) of Fig. 6 for the stratified and unstratified cases, respectively. This can be explained by the decrease in the disc density n due to its expansion in the stratified runs. Finally, in both cases the plasma beta $\overline{\beta}$ ($\equiv \langle 8\pi P\rangle_v/\langle B^2\rangle_v$) reaches a nearly steady state regime for $t \gtrsim 3$ $[2\pi/\Omega_0]$, as shown by the dashed lines in panel (a) of Fig. 6. However, while $\overline{\beta} \sim 2$ in the unstratified case, $\overline{\beta} \sim 0.4$ in the stratified case, which shows that stratification produces a disc that is magnetic-pressure supported, consistently with previous MHD stratified simulations (Bai & Stone 2013; Salvesen et al. 2016).

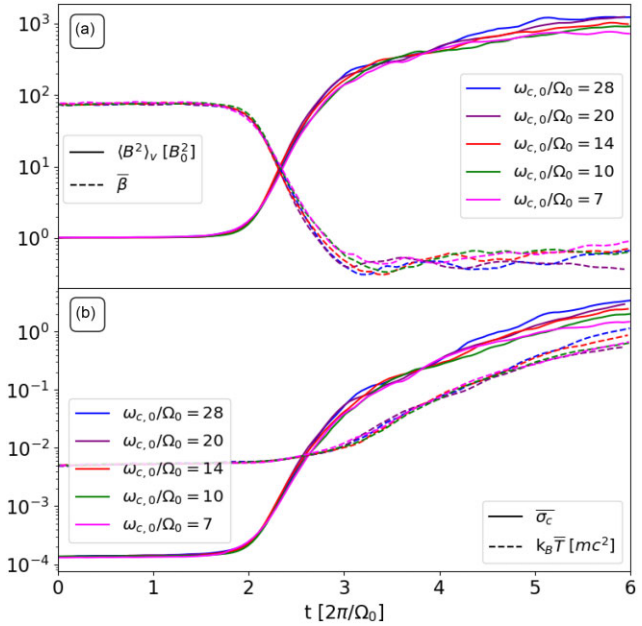

Figure 7. Plasma properties as a function of time t for the disc region of 2D stratified runs using $\omega_{c,0}/\Omega_0 = 7$, 10, 14, 20, and 28. Panel (a) shows $\langle B^2\rangle_v$ (solid) and $\overline{\beta}$ (dashed). Panel (b) shows $\overline{\sigma}_c$ (solid) and $\overline{T}$ (dashed).

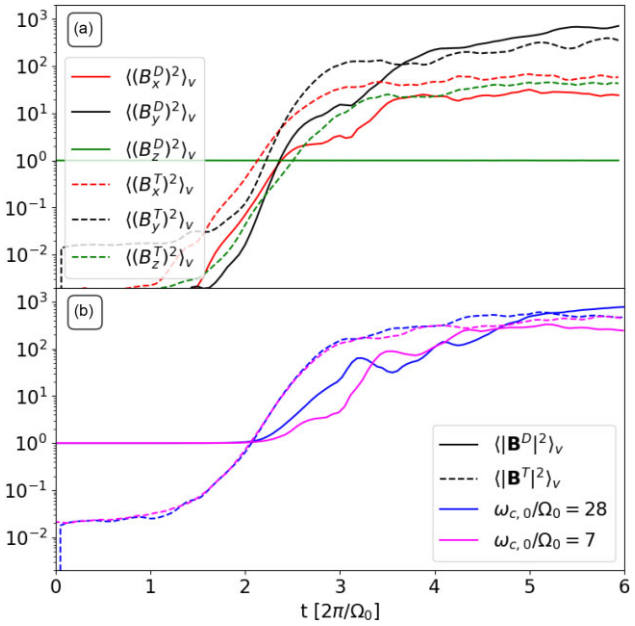

Figure 8. Panel (a): the solid lines show $\langle(B_x^D)^2\rangle_v$, $\langle(B_y^D)^2\rangle_v$, and $\langle(B_z^D)^2\rangle_v$, respectively, for run ST2D-20 ($\omega_{c,0}/\Omega_0 = 20$). The dashed lines show $\langle(B_x^T)^2\rangle_v$, $\langle(B_y^T)^2\rangle_v$, and $\langle(B_z^T)^2\rangle_v$ for the same run and in the same region. Panel (b): the total energies in the dynamo-like field $\mathbf{B}^D$ (solid line) and in the turbulent field $\mathbf{B}^T$ (dashed line) for the runs ST2D-20 ($\omega_{c,0}/\Omega_0 = 28$) and ST2D-7 ($\omega_{c,0}/\Omega_0 = 7$).

In order to explore the role of the scale-separation ratio $\omega_{c,0}/\Omega_0$ in our stratified runs, panels (a) and (b) of Fig. 7 show the quantities $\langle B^2\rangle_v$, $\overline{\beta}$, $\overline{\sigma}_c$, and $\overline{T}$ for stratified simulations with $\omega_{c,0}/\Omega_0 = 7$, 10, 14, 20, and 28. We see that increasing $\omega_{c,0}/\Omega_0$ produces a slight increase in $\langle B^2\rangle_v$ and $\overline{\sigma}_c$, not yet showing a clear convergence for the highest values of $\omega_{c,0}/\Omega_0$. (Note that the time origins of these simulations were slightly adjusted to align their exponential growth temporally, facilitating comparison.) The evolutions of $\overline{T}$ and $\overline{\beta}$ exhibit some variations within a factor of $\sim$2, but without showing a discernible dependence on $\omega_{c,0}/\Omega_0$. Also, in Appendix A we use the case $\omega_{c,0}/\Omega_0 = 20$ to show that these results are not affected by the spatial resolution of our runs.

As discussed in Section 3.1, another important feature of the stratified 2D simulations is a dynamo-like action that produces a significant $B_y^D = \langle B_y\rangle_x$ field, as shown in panels (a) and (b) of Fig. 2. The magnetic energy in the disc provided by the dynamo-like field $\mathbf{B}^D$ in run ST2D-20 is shown by the solid lines in the panel (a) of Fig. 8, where the red-solid, black-solid, and green-solid lines show the contributions by the three components of $\mathbf{B}^D$: $\langle(B_x^D)^2\rangle_v$, $\langle(B_y^D)^2\rangle_v$, and $\langle(B_z^D)^2\rangle_v$, respectively. We see that the dynamo-like action within the disc is indeed dominated by the toroidal component of the magnetic field. Panel (a) of Fig. 8 also shows in dashed lines the contribution to the magnetic energy provided by the three components of the turbulent magnetic field $\boldsymbol{B}^T$, which are averaged over the disc volume obtaining $\langle(B_x^T)^2\rangle_v$, $\langle(B_y^T)^2\rangle_v$, and $\langle(B_z^T)^2\rangle_v$ (red-dashed, black-dashed, and green-dashed lines, respectively). We see that the turbulent field is dominated by its toroidal component as well and contributes most of the magnetic energy in the disc from the triggering of the MRI turbulence at $t \approx 2$ [$2\pi/\Omega_0$] until $t \approx 3.5$ [$2\pi/\Omega_0$]. After that, the toroidal component of the dynamo-like field $\langle\langle B_y\rangle_x^2\rangle_z$ becomes larger (by a factor of $\sim$2) than the toroidal component of the turbulent field.

Panel (b) of Fig. 8 shows the total energies in the dynamo-like field $\mathbf{B}^D$ (blue-solid line) and in the turbulent field $\mathbf{B}^T$ (blue-dashed line) for run ST2D-20 ($\omega_{c,0}/\Omega_0 = 20$). We see that after $t \approx 4$ [$2\pi/\Omega_0$] the energies in the dynamo and turbulent fields are comparable. Thus, in terms of the total magnetic energy, the dynamo-like and turbulent magnetic fields are roughly equally important after the initial period (of $\sim$1 orbit after the triggering of the MRI) in which the turbulent magnetic energy dominates. This trend appears to not be significantly affected by the scale-separation ratio $\omega_{c,0}/\Omega_0$. This is shown by the pink-solid and pink-dashed lines in panel (b) of Fig. 8, which show the contributions by, respectively, the turbulent and dynamo-like fields to the magnetic energy in the disc of run ST2D-7 ($\omega_{c,0}/\Omega_0 = 7$). We see that in this $\omega_{c,0}/\Omega_0 = 7$ run there is also an initial period of about $\sim$1 orbit in which the turbulent field energy dominates, followed by a similar contribution to energy by the turbulent and dynamo-like fields.

Thus, we have shown that disc stratification in 2D can change significantly the behaviour of the MRI turbulence compared to the unstratified case. Besides producing significant outflows and a puffing up of the disc due to temperature increase, stratification makes the disc turbulence more magnetically dominated (smaller β) compared to what is shown in an analogous 2D unstratified simulation. Stratification also gives rise to a significant large-scale dynamo-like activity, which contributes similarly to the magnetic energy in the non-linear MRI stage as the turbulent field after $\sim$1 orbit from the triggering of the MRI. We also found that increasing the scale-separation ratio produces slightly more magnetized discs, obtaining no complete convergence for the largest values of $\omega_{c,0}/\Omega_0$ used, consistent with the result obtained by Bacchini et al. (2022) who found that a scale-separation ratio $\omega_{c,0}/\Omega_0 \gtrsim 60$ is required for a complete convergence in the 2D case.

In the next section, we compare these 2D results with a 3D simulation showing that, although some differences appear, most of our 2D results are reasonably well reproduced in the 3D case.

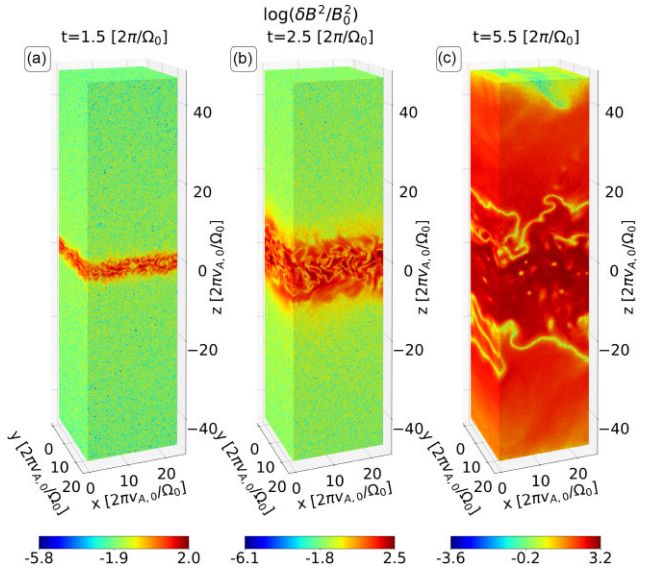

Figure 9. Panels (a)–(c) show δB^2 for simulation ST3D-3.5 at $t = 1.5$, 2.5, and 4.5 $[2\pi/\Omega_0]$, respectively.

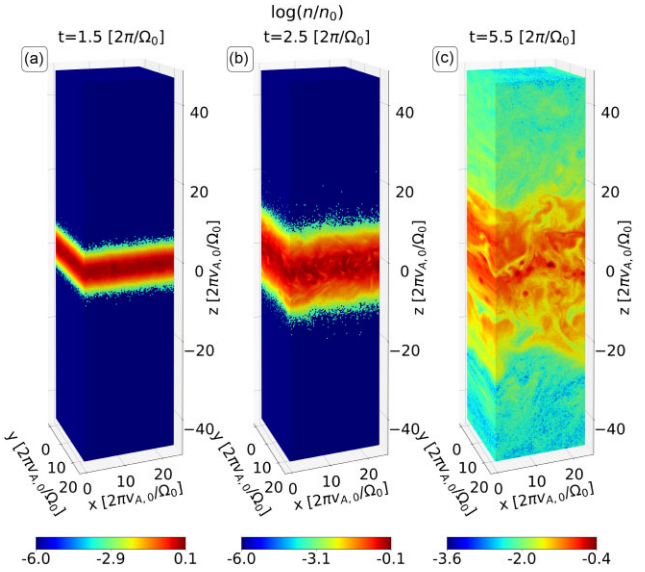

Figure 10. Panels (a)–(c) show n for simulation ST3D-3.5 at $t = 1.5$, 2.5, and 4.5 $[2\pi/\Omega_0]$, respectively.

4 3D MRI TURBULENCE

In this section, we present results from a 3D stratified simulation, run ST3D-3.5 ($\omega_{c,0}/\Omega_0 = 3.5$) and compare them with the analogous 2D stratified run ST2D-3.5. Given their small-scale separation, we use these runs only as an initial attempt to assess the importance of 3D effects. Thus, our 3D run ST3D-3.5 is not intended to provide definitive answers regarding the 3D behaviour of the MRI turbulence.

4.1 Turbulence properties in 2D versus 3D

Fig. 9 shows three snapshots of δB^2 for the stratified 3D run ST3D-3.5 at times $t = 1.5$, 2.5, and 5.5 $[2\pi/\Omega_0]$. At the qualitative level, there are many similarities with the turbulence structure of the 2D runs. At $t = 1.5$ $[2\pi/\Omega_0]$, non-linear channel flows are present in δB^2, which look similar to the ones shown in panel (a) of Fig. 1 for run ST2D-20. At $t = 2.5$ $[2\pi/\Omega_0]$, the channel flows have already reconnected and broken into turbulence, with a significant increase in the disc thickness, similarly to what was shown for run ST2D-20 in panel (c) of Fig. 1. This trend continues at later times, as can be seen in panel (c) of Fig. 9, which shows δB^2 at $t = 5.5$ $[2\pi/\Omega_0]$. Fig. 10 shows the same snapshots of Fig. 9, but for the particle density n. At $t = 1.5$ $[2\pi/\Omega_0]$ non-linear channel flows are present in n, similarly to what is shown in panels (b) of Fig. 1 for run ST2D-20. At $t =$ 2.5 and 4 $[2\pi/\Omega_0]$, a much more turbulent and progressively thicker disc is shown, as also shown for run ST2D-20 in panels (d) and (f) of Fig. 1.

Our 3D run also shows the action of a dynamo-like mechanism, as can be seen from panel (d) of Fig. 2, which shows B_y averaged over the x–y plane, $\langle B_y \rangle_{x-y}$, as a function of time t and of the vertical coordinate z. We see that a net $\langle B_y \rangle_{x-y}$ field is formed, with an amplitude similar to the 2D cases shown in panels (a) and (b) of Fig. 2 (runs ST2D-20 and ST2D-3.5). However, while the dynamo-like field in 2D shows significant time-variability and inhomogeneity along the z-coordinate, in 3D this field appears less variable and more homogeneous.

The behaviour of the magnetic power spectrum seems to be quite similar in 2D and 3D. Panels (a) and (b) of Fig. 11 compare, respectively, the poloidal and toroidal magnetic spectra of the 2D and

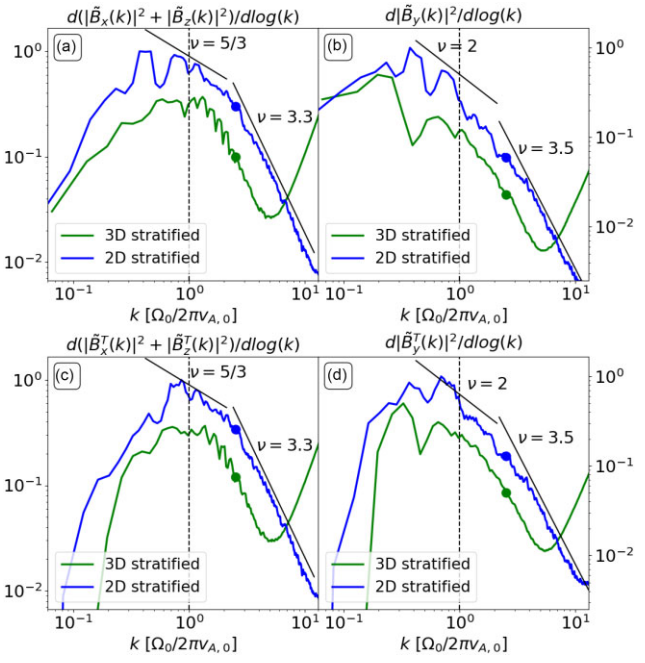

Figure 11. Panels (a) and (b) show the power spectra of the poloidal and toroidal components of the magnetic field, $d(|\tilde{B}_x(k)|^2 + |\tilde{B}_z(k)|^2)/dln(k)$ and $d|\tilde{B}_y(k)|^2/\mathrm{dln}(k)$, respectively, for the 2D and 3D stratified runs ST2D-3.5 and ST3D-3.5. Panels (c) and (d) show the same as in panels (a) and (b), respectively, but considering only the turbulent field $\mathbf{B}^T$.

3D runs ST3D-3.5 and ST2D-3.5 (blue and green lines, respectively). These runs share the same ratio $\omega_{c,0}/\Omega_0 = 3.5$, so that the effect of the scale-separation does not affect significantly the comparison. At sub-Larmor scales ($k\rho_l > 1$, where $k\rho_l = 1$ is marked by the coloured dots on each line), we observe a magnetic spectrum with $\nu \approx 3.3$ (poloidal case) and $\nu \approx 3.5$ (toroidal case), for both types of runs. These $\nu \approx 3.3$ and 3.5 spectra are, however, steeper than the ones shown by the 2D runs with higher $\omega_{c,0}/\Omega_0$, showing that a minimum scale-separation ratio is necessary for correctly capturing

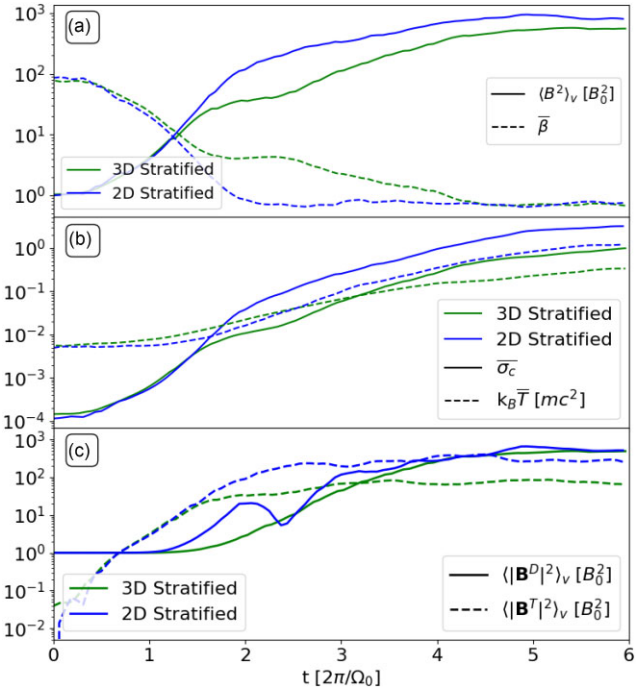

Figure 12. Average disc plasma properties as as a function of time t for 2D and 3D stratified runs ST2D-3.5 and ST3D-3.5, respectively. Panel (a) shows $\langle B^2\rangle_v$ (solid) and $\overline{\beta}$ (dashed). Panel (b) shows $\overline{\sigma}_c$ (solid) and $\overline{T}$ (dashed). Panel (c) shows the magnetic energy densities in the turbulent field $|\mathbf{B}^T|^2$ (dashed) and in the dynamo-like field $|\mathbf{B}^D|^2$ (solid) in 2D and 3D.

the behaviour of the sub-Larmor part of the spectra. Above Larmor scales ($k\rho_l < 1$), both runs show a poloidal and toroidal magnetic field spectra with ν close to $\nu \approx 5/3$ and ≈ 2, respectively. These $\nu \approx 5/3$ and ≈ 2 behaviours are maintained when removing the dynamo-like field in both runs (which in 3D is defined as in equation (15) but with $\mathbf{B}^D \equiv \langle\mathbf{B}\rangle_{x-y}$). This is shown in panels (c) and (d) of Fig. 11 where we show the poloidal and toroidal spectra of $\mathbf{B}^T$. The main effect of removing $\mathbf{B}^D$ is to substantially reduce the contribution of $k\,2\pi\,v_{A,0}/\,\Omega_0 \lesssim 1$ to the toroidal part of the 2D and 3D spectra. In this way, the peak of the poloidal and toroidal spectra of $\mathbf{B}^T$ both in 2D and 3D approach $k\,2\pi\,v_{A,0}/\,\Omega_0 \sim 1$ (although the toroidal part of the turbulent spectrum in 3D has its peak at wavelengths $\sim$3 times larger than in 2D). This behaviour of the $\mathbf{B}^T$ spectra in runs ST3D-3.5 and ST2D-3.5 above Larmor scales is similar to the ones shown in our stratified 2D runs with higher scale-separation ratio (Fig. 4), as well as in previous unstratified MHD (Walker et al. 2016) and kinetic 3D simulations (Kunz et al. 2016; Bacchini et al. 2022).

4.2 Disc plasma properties in 2D vs 3D

In this section, we compare the disc plasma properties evolution in 2D and 3D. Panel (a) in Fig. 12 shows the evolution of $\langle B^2\rangle_v$ in the 2D and 3D runs ST2D-3.5 and ST3D-3.5. In both cases, there is an initial exponential growth regime that evolves into a non-linear regime with a much smaller growth rate at $t \approx 1.5$ [$2\pi/\Omega_0$]. Later, in the time interval $t \sim 1.5$–3 [$2\pi/\Omega_0$], significant differences appear in the 2D and 3D cases, with the 3D run having a $\langle B^2\rangle_v$ amplitude $\sim$5 times smaller. This significant difference in $\langle B^2\rangle_v$ produces a similar difference in $\overline{\sigma}_c$, as can be seen from the solid blue and green lines in panel (b) of Fig. 12. This implies that in that time interval the disc expansion (and therefore its density) is about the same in the two simulations. This is consistent with the fact that their temperatures $\overline{T}$ reach similar values, as shown by the dashed lines in panel (b) of Fig. 12. Finally, consistently with the behaviours of $\overline{T}$ and $\overline{\sigma}_c$, $\overline{\beta}$ is $\sim$5 times larger in the 3D case during the time period $t \sim 1.5$–3.5 [$2\pi/\Omega_0$]. Later, when $t \gtrsim 3$ [$2\pi/\Omega_0$] there is a transition towards a state in which the amplitudes of $\langle B^2\rangle_v$ in 2D and 3D tend to give more similar values, which also tends to produce similar values of $\overline{\beta}$. Indeed, for $t \gtrsim 4$ [$2\pi/\Omega_0$], $\overline{\beta} \approx 0.5$ in both runs while $\langle B^2\rangle_v$ is only a factor of $\sim$2 larger in the 2D case.

The smaller magnetic amplification shown by the 3D run in the time interval $t \sim 1.5$–4 [$2\pi/\Omega_0$] is consistent with recent unstratified PIC simulations of the MRI that show that using 3D runs is important to allow the reconnection of the toroidal magnetic field component (Bacchini et al. 2022). By the end of the simulations, however, the 2D and 3D magnetic energies only differ by a factor of $\sim$2. This can be explained by the growing importance of the dynamo-like field in the stratified 2D and 3D runs, which evolves very similarly in these two types of runs. The progressively growing importance of the dynamo-like field in 2D can be seen from panel (c) of Fig. 12, which shows that in run ST2D-3.5, $|\mathbf{B}^D|^2$ (solid-blue line) starts smaller than the turbulent part of the magnetic energy density $|\mathbf{B}^T|^2$ (dotted-blue line) for $t \lesssim 4$ [$2\pi/\Omega_0$], but afterwards it becomes comparable to $|\mathbf{B}^T|^2$. This is indeed consistent with what was shown for 2D runs with larger scale-separation ratios in Fig. 8. In the 3D run ST3D-3.5, this increase in the dynamo-like field importance is even more significant, since $|\mathbf{B}^D|^2$ (solid-green line) becomes $\sim$5 times larger than $|\mathbf{B}^T|^2$ (dotted-green line) at $t \gtrsim 4$ [$2\pi/\Omega_0$], given that 3D runs dissipate $|\mathbf{B}^T|^2$ more efficiently via reconnection. Since $|\mathbf{B}^D|^2$ has essentially the same values in 2D and 3D, it is thus expected that, by the end of the simulations, $\langle B^2\rangle_v$ only differs by a factor of $\sim$2 between the 2D and 3D cases.

In Section 5.2, we show that the similitude between 2D and 3D by the end of the runs is also reproduced when analysing the MRI-driven effective viscosity.

5 EFFECTIVE VISCOSITY

In this section, we analyse the effective disc viscosity caused by the MRI turbulence. This viscosity is quantified making used of the α parameter (Shakura & Sunyaev 1973), defined as the xy component of the plasma stress tensor T_{xy}, normalized by the plasma pressure, $\alpha = T_{xy}/P$. This stress tensor component T_{xy} has three contributions: the Maxwell stress $M_{xy} = -B_xB_y/4\pi$, the Reynolds stress $R_{xy} = mnV_xV_y$, where $\boldsymbol{V} = (V_x, V_y, V_z)$ is the fluid velocity, and the anisotropic stress $A_{xy} = -(P_\perp - P_\parallel)B_xB_y/B^2$, where $P_\perp$ and $P_\parallel$ are the plasma pressures perpendicular and parallel to the local magnetic field. Notice that, even though in the calculation of R_{xy} we assume non-relativistic fluid velocities, in our simulations individual particles can still acquire relativistic velocities. Thus, $\boldsymbol{V}$ is calculated as $\boldsymbol{V} = \langle\boldsymbol{p}\rangle_p/m\langle\gamma\rangle_p$, where $\boldsymbol{p}$ and γ are the momenta and Lorentz factors of the particles in a given fluid element and $\langle\,\rangle_p$ denotes an average over those particles. In this way, we ensure that the fluid velocity $\boldsymbol{V}$ corresponds to the velocity of the reference frame where the average particles momentum within a fluid element vanishes.

5.1 Effect of stratification and $\omega_{c,0}/\Omega_0$ on viscosity

Fig. 13 shows in solid blue line the time evolution of the average parameter $\overline{\alpha}$ ($\equiv \langle T_{xy}\rangle_v/\langle P\rangle_v$) for run ST2D-20, along with the contributions from the Maxwell, Reynolds, and anisotropic stresses: $\overline{\alpha}_M$ ($\equiv \langle M_{xy}\rangle_v/\langle P\rangle_v$; dotted blue line), $\overline{\alpha}_R$ ($\equiv \langle R_{xy}\rangle_v/\langle P\rangle_v$; dotted–dashed blue line) and $\overline{\alpha}_A$ ($\equiv \langle A_{xy}\rangle_v/\langle P\rangle_v$; dashed line), respec-

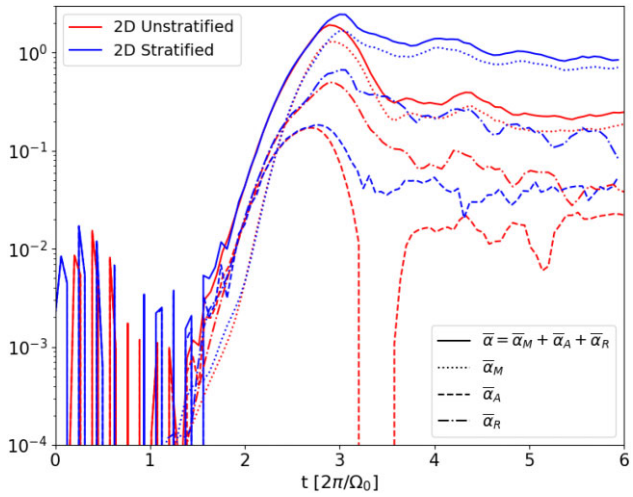

Figure 13. The solid lines show the evolution of $\overline{\alpha}$ in the stratified run ST2D-20 and the unstratified run UN2D-20. The contributions from the Maxwell, Reynolds, and anisotropic stresses ($\overline{\alpha}_M$, $\overline{\alpha}_R$, and $\overline{\alpha}_A$, respectively) are also shown by the dotted, dashed–dotted, and dashed lines, respectively.

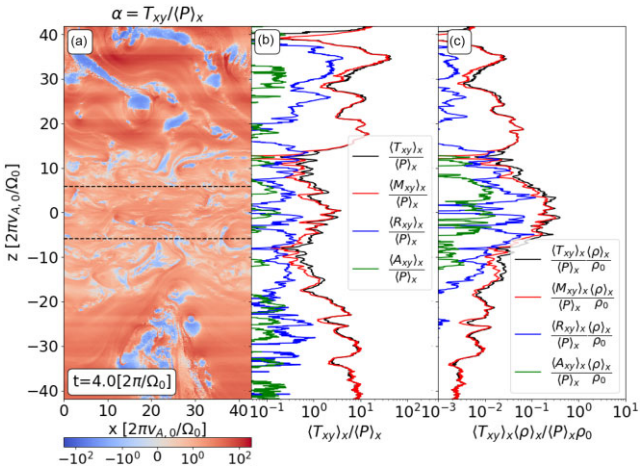

Figure 14. Panel (a) shows the 2D map of the total $\alpha(\equiv T_{xy}/\langle P\rangle_x)$ parameter in the stratified run ST2D-20 at time $t = 4$ $[2\pi/\Omega_0]$, the horizontal black dashed lines represent the disc region at that time. Panel (b) shows the horizontally integrated α parameter and the Maxwell, Reynolds and anisotropic stresses contribution are also shown.

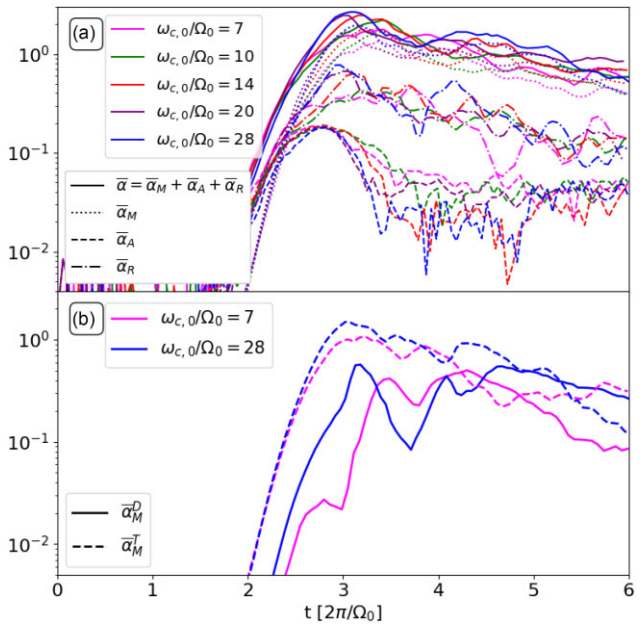

Figure 15. Panel (a) shows in solid lines the evolution of $\overline{\alpha}$ in 2D runs with $\omega_{c,0}/\Omega_0 = 7$ (ST2D-7), $\omega_{c,0}/\Omega_0 = 10$ (ST2D-10), 14 (ST2D-14), 20 (ST2D-20), and 28 (ST2D-28). The corresponding contributions from the Maxwell, Reynolds, and anisotropic stresses ($\overline{\alpha}_M$, $\overline{\alpha}_R$, and $\overline{\alpha}_A$, respectively) are also shown by the dotted, dashed–dotted, and dashed lines, respectively. Panel (b) shows the contribution to $\overline{\alpha}_M$ by the turbulent field $\mathbf{B}^T$ (dashed lines) and dynamo-like fields $\mathbf{B}^D$ (solid lines) in runs ST2D-28 run ($\omega_{c,0}/\Omega_0 = 28$) and ST2D-7 ($\omega_{c,0}/\Omega_0 = 7$) , which we name $\overline{\alpha}_M^T$ and $\overline{\alpha}_M^D$, respectively.

tively. We see that $\overline{\alpha}$ reaches a saturated value of $\overline{\alpha} \sim 1$, which is dominated by the Maxwell stress, with the contributions to $\overline{\alpha}$ following the ordering $\overline{\alpha}_M > \overline{\alpha}_R > \overline{\alpha}_A$. The fact that $\overline{\alpha}_M \sim 1$ is consistent with the dominance of magnetic pressure compared to particle pressure ($\overline{\beta} \lesssim 1$) seen in panel (a) of Fig. 6 for the same run ST2D-20. We compare these results with the ones of the analogous unstratified run UN2D-20, where we find a similar ordering of the contributions to $\overline{\alpha}$, $\overline{\alpha}_M > \overline{\alpha}_R > \overline{\alpha}_A$, but with a ∼4 times smaller $\overline{\alpha}_M$. This difference is consistent with the ∼4 times larger $\overline{\beta}$ obtained in the unstratified run, implying a significant effect of stratification on the disc viscosity in collisionless studies of the MRI. Notably, the importance of $\overline{\alpha}_R$ in our results seems to contradicts previous unstratified kinetic studies (Kunz et al. 2016; Bacchini et al. 2022), but are in line with the findings from stratified MHD simulations (Bai & Stone 2013; Salvesen et al. 2016).

Including stratification also allows capturing the different behaviours of the effective viscosity as a function of the z coordinate. Panel (a) of Fig. 14 shows the 2D map of the effective α viscosity for run ST2D-20 at time $t = 4$ $[2\pi/\Omega_0]$. This viscosity is computed as the ratio between the total stress tensor (T_{xy}) on each grid, divided by the the plasma pressure averaged along the x-axis ($\langle P\rangle_x$) (the horizontal dashed black lines denote the disc region). As can be seen, the effective viscosity at $|z| \gtrsim 2H(\overline{T})$ is significantly larger than in the disc region, consistent with the idea that accretion can proceeds more efficiently through surface layers around the disc (Rothstein & Lovelace 2008; Guilet & Ogilvie 2012; Jacquemin-Ide, Lesur & Ferreira 2021). This is confirmed in panel (b) of Fig. 14, which shows the radially averaged viscosity $\langle T_{xy}\rangle_x/\langle P\rangle_x$, disaggregated by its contributions from the Maxwell, Reynolds, and anisotropic stresses. Both within and outside the disc, $\langle T_{xy}\rangle_x/\langle P\rangle_x$ is dominated by the Maxwell stress, which increases about one order of magnitude away from the disc. This increase in the viscosity outside the disc is expected to significantly increase the advection of magnetic flux, although, due to the low-mass density in this region, it should have a secondary impact on the overall mass accretion rate. This can be seen in panel (c) of Fig. 14, where the different contributions to the effective disc viscosity are multiplied by the radially averaged plasma density $\langle\rho\rangle_x$ normalized by ρ_0.

We also measured the effect of $\omega_{c,0}/\Omega_0$ on the behaviour of $\overline{\alpha}_M$, $\overline{\alpha}_R$, $\overline{\alpha}_A$, and the total $\overline{\alpha}$, which is done in panel (a) of Fig. 15. We see that, although $\overline{\alpha}$ fluctuates by factors of order unity, there is no discernible dependence of this quantity on ω_c/Ω_0, implying that the scale separation used in our 2D runs appears to be large enough to accurately capture the behaviour of the MRI-driven viscosity. The blue lines in panel (b) of Fig. 15 also compare the contribution to $\overline{\alpha}_M$ by the turbulent field $\mathbf{B}^T$ (dashed lines) and dynamo-like fields $\mathbf{B}^D$

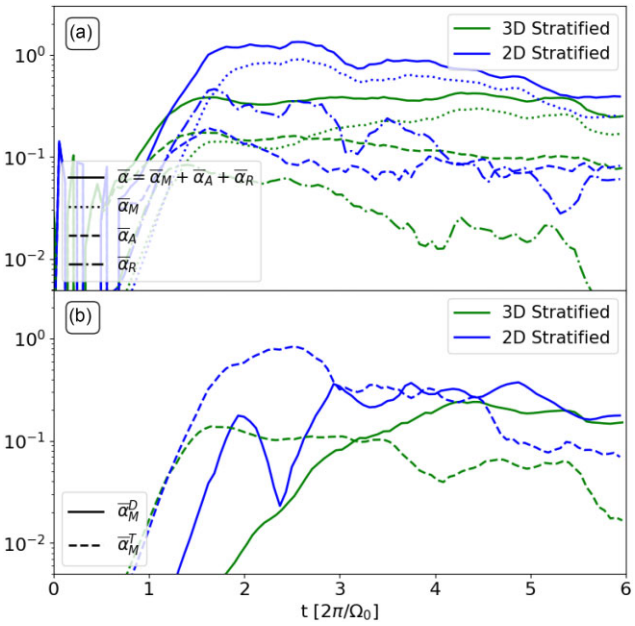

Figure 16. Panel (a) shows in solid lines the evolution of $\overline{\alpha}$ in the 3D run ST3D-3.5 and the 2D run ST2D-3.5. Their contributions from the Maxwell, Reynolds, and anisotropic stresses ($\overline{\alpha}_M$, $\overline{\alpha}_R$, and $\overline{\alpha}_A$, respectively) are also shown by the dotted, dashed–dotted, and dashed lines, respectively. Panel (b) shows the contributions of the dynamo-like magnetic field (solid) and the turbulent magnetic field (dashed) to the Maxwell stress, $\overline{\alpha}_M^D$ and $\overline{\alpha}_M^T$, in the 3D run ST3D-3.5 and the 2D run ST2D-3.5.

(solid lines) in the ST2D-28 run ($\omega_{c,0}/\Omega_0 = 28$), which we name $\overline{\alpha}_M^T$ and $\overline{\alpha}_M^D$, respectively. We see that $\overline{\alpha}_M^T$ dominates until $t \sim 4$ [$2\pi/\Omega_0$]. After that moment $\overline{\alpha}_M^T$ and $\overline{\alpha}_M^D$ are comparable, with fluctuating differences of a factor ∼2–3). A similar behaviour is obtained for $\overline{\alpha}_M^T$ and $\overline{\alpha}_M^D$ in run ST2D-7 ($\omega_{c,0}/\Omega_0 = 7$), which are shown by dashed-pink and solid-pink lines, respectively. This implies that no clear effect of the scale-separation ratio of $\overline{\alpha}_M^T$ and $\overline{\alpha}_M^D$ is observed in our simulations. The fact that these quantities become comparable after $t \sim 4$ [$2\pi/\Omega_0$] is in line with the behaviours of $|\mathbf{B}^T|^2$ and $|\mathbf{B}^D|^2$ for runs ST2D-28 and ST2D-7, which also become comparable in the same time period, as shown in panel (b) of Fig. 8.

5.2 Viscosity in 2D versus 3D

Panel (a) of Fig. 16 compares the effective viscosities of the 3D and 2D runs ST3D-3.5 and ST2D-3.5, respectively. We see that for $t \gtrsim 1.5$ [$2\pi/\Omega_0$], the viscosity of the 3D run has a nearly steady value of $\overline{\alpha} \approx 0.5$. For $t \sim 1.5$–3.5 [$2\pi/\Omega_0$], the 3D $\overline{\alpha}$ is ∼3–4 times smaller than in the 2D case, while for $t \gtrsim 3.5$ [$2\pi/\Omega_0$] the $\overline{\alpha}$ of the 2D and 3D runs become more similar, differing by a maximum factor of ∼2. The time dependence of the difference between the 2D and 3D values of $\overline{\alpha}$ is consistent with the fact that, initially, the 3D $\overline{\beta}$ is ∼3–5 times larger than in 2D, with a subsequent period at $t \gtrsim 3.5$ [$2\pi/\Omega_0$] in which both $\overline{\alpha}$'s acquire essentially the same value, as shown by the dashed blue (2D) and green (3D) lines in panel (a) of Fig. 12.

These results reinforce the idea that, when the dynamo-like field becomes either dominant (3D) or comparable to the turbulent field (2D) at $t \gtrsim 3.5$ [$2\pi/\Omega_0$], the 2D and 3D runs produce fairly similar results, which include the value of the (Maxwell stress-dominated) disc viscosity. When that happens, $\overline{\alpha}_M$ itself is significantly affected by the dynamo-like field. This can be seen from panel (b) of Fig. 16, which shows the contributions of the dynamo-like magnetic field

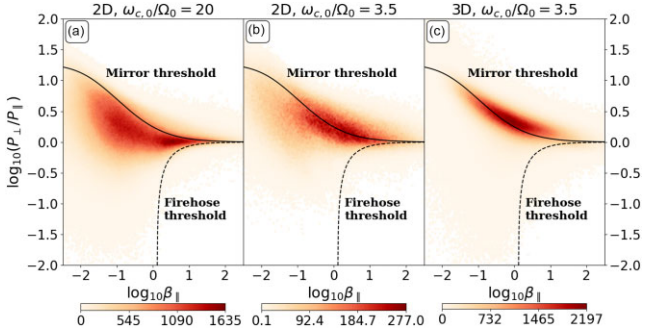

Figure 17. Panels (a)–(c) show the distributions of plasma anisotropy $P_\perp/P_\parallel$ and $\beta_\parallel$ in the disc of the 2D run ST2D-20 during $t = 3.5 - 4.5$ [$2\pi/\Omega_0$], the 2D run ST2D-3.5 during $t = 2.5 - 3.5$ [$2\pi/\Omega_0$], and the 3D run ST3D-3.5 during $t = 2 - 3$ [$2\pi/\Omega_0$], respectively. The three cases are compared with a threshold for the growth of unstable mirror modes (black line) and firehose modes (dashed line) obtained from linear Vlasov theory (Hellinger et al. 2006).

(solid) and the turbulent magnetic field (dashed) to the Maxwell stress, $\overline{\alpha}_M^D$ and $\overline{\alpha}_M^T$, in the 3D run ST3D-3.5 (green) and the 2D run ST2D-3.5 (blue). At $t > 3.5$ [$2\pi/\Omega_0$], the 3D run exhibits a greater contribution to the Maxwell stress attributed to the dynamo-like field (by a factor ∼5). This dominant contribution to the viscosity by the large-scale dynamo-like field is in qualitative agreement with the 3D MHD simulations of Bai & Stone (2013) in the case of $\beta_0 = 100$. Conversely, in the 2D run ST2D-3.5 the dynamo-like contribution to the viscosity becomes comparable to the one of the turbulent field after $t \sim 3.5$ [$2\pi/\Omega_0$], with some dominance of the former after $t \sim 4.5$ [$2\pi/\Omega_0$] by a factor of ∼2–3. This is in line with results shown for the 2D runs ST2D-28 and ST2D-7 ($\omega_{c,0}/\Omega_0 = 28$ and 7, respectively), for which $\overline{\alpha}_M^D$ and $\overline{\alpha}_M^T$ were comparable after $t \sim 4$ [$2\pi/\Omega_0$], with no discernible dependence on $\omega_{c,0}/\Omega_0$.

Both our 2D and 3D runs give rise to an anisotropic stress that is subdominant compared to the Maxwell stress, although the former is larger than the Reynolds stress in the 3D run, which is the contrary to what occurs in 2D, suggesting that 3D effects would tend to suppress the fluid velocities that give rise to the Reynolds stress.

5.3 Pressure anisotropy behaviour

The very small contribution of $\overline{\alpha}_A$ to the total effective viscosity in our 2D and 3D stratified runs seems to contradict previous kinetic simulation studies that suggest that the anisotropic stress can be as important as Maxwell stress in collisionless discs (e.g. Kunz et al. 2016). This discrepancy, however, appears to be mainly due to the small β regime reached in the non-linear state of our simulations. To demonstrate this point, panel (a) of Fig. 17 shows the distribution of plasma anisotropy $P_\perp/P_\parallel$ and $\beta_\parallel$ in the disc of run ST2D-20 during a time interval $t = 3.5 - 4.5$ [$2\pi/\Omega_0$], and compares it with a threshold for the growth of unstable mirror modes (black line) obtained from linear Vlasov theory (Hellinger et al. 2006):

$$\frac{P_\perp}{P_\parallel} = 1 + \frac{0.77}{(\beta_\parallel - 0.016)^{0.76}}. \quad (16)$$

We see that in most cases $P_\perp/P_\parallel$ tends to be larger than unity and limited by the mirror threshold. As an estimate of the upper limit for the expected importance of α_A, one can compute the ratio $\langle \alpha_A/\alpha_M \rangle_v$ assuming that the pressure anisotropy of the plasma is given by

equation (16). In that case we would have

$$\left\langle \frac{\alpha_A}{\alpha_M} \right\rangle_v = \left\langle \frac{(P_\perp - P_\parallel)}{P_\parallel} \frac{\beta_\parallel}{2} \right\rangle_v \lesssim 0.4 \langle \beta_\parallel^{0.24} \rangle_v \sim 0.4 (\overline{\beta}_\parallel)^{0.24}, \quad (17)$$

where we have applied equation (16) in the limit $\beta_\parallel \gg 0.016$ ($\overline{\beta}_\parallel \approx 0.4$ for $t \gtrsim 3$ $[2\pi/\Omega_0]$, as can be seen from the $\overline{\beta}_\parallel$ evolution for run ST2D-20 shown in Fig. 6). Thus, using $\overline{\beta}_\parallel \approx 0.4$, we obtain $\langle \alpha_A/\alpha_M \rangle_v \lesssim 0.3$. This upper limit is consistent with the fact that $\overline{\alpha}_A$ is much smaller (by a factor of $\sim$10) than $\overline{\alpha}_M$ in run ST2D-20, as shown, respectively, by the dashed blue and dotted blue lines in Fig. 13. Notice that in a hypothetical case in which $\overline{\beta}_\parallel \sim 100$ (e.g. as in Kunz et al. 2016), equation (17) would predict comparable contributions from the anisotropic and Maxwell stress with $\overline{\alpha}_A \sim \overline{\alpha}_M$.

Panel (b) of Fig. 17 shows the same as panel (a), but for the 2D run ST2D-3.5. We see that $P_\perp/P_\parallel$ is somewhat larger in the case of run ST2D-3.5 for a given $\beta_\parallel$. The larger value of $P_\perp/P_\parallel$ is consistent with the smaller scale-separation ratio, as shown by previous PIC simulation studies of the mirror instability driven by a growing background magnetic field (see e.g. Ley et al. 2023). However, the distribution of $P_\perp/P_\parallel$ and $\beta_\parallel$ in the disc of run ST2D-3.5 still follows reasonably well the threshold for the growth of mirror modes presented in equation (16), consistently with the essentially absent effect of scale-separation on the dominance of $\overline{\alpha}_M$ in our runs. Panel (c) of Fig. 17 shows the behaviour for $P_\perp/P_\parallel$ and $\beta_\parallel$ in the 3D run ST3D-3.5. We see that the pressure anisotropy behaves similarly in the runs ST2D-3.5 and ST3D-3.5, in agreement with the small contribution of $\overline{\alpha}_A$ to the effective viscosity in the 3D case.

In summary, our 2D and 3D runs give a (Maxwell stress dominated) $\overline{\alpha}$ with values between $\sim$0.5 (3D) and $\sim$1 (2D), with a progressively similar behaviour of the 2D and 3D runs as the dynamo-like field becomes dominant ($t \gtrsim 3.5$ $[2\pi/\Omega_0]$). In this dynamo-dominated regime, $\overline{\alpha}$ is expected to be mainly produced by the dynamo-like field. Interestingly, this viscosity behaviour is very similar to the one obtained from 3D MHD simulations of stratified disc with net vertical field and initial $\beta = 100$ (Salvesen et al. 2016).

6 PARTICLE ACCELERATION

Our stratified MRI simulations show significant particle acceleration. In this section, we show that the acceleration efficiency grows as the disc temperature and the scale-separation ratio $\omega_{c,0}/\Omega_0$ increase. Well developed non-thermal tails are observed mainly in our 2D runs, due to their relatively large scale-separation ratio.

6.1 Spectrum evolution in 2D

The evolution of the particle spectrum, $\mathrm{d}n/\mathrm{d}\gamma$, calculated in the disc of run ST2D-20 is shown in Fig. 18, where γ is the particle Lorentz factor in the local fluid frame, substracting the bulk velocity of the plasma. The spectra are shown for different values of the disc temperature $\overline{T}$, instead of at different times. (This allows us to compare spectra from different simulations, removing the fact that different runs may take different times to trigger the MRI and/or to heat the plasma.) As the plasma temperature increases, their spectra develop a nonthermal tail that can be approximately described as a power law with an exponential cut-off,

$$\frac{\mathrm{d}n}{\mathrm{d}\gamma} \propto (\gamma - 1)^{-p} e^{-\gamma/\gamma_c}, \quad (18)$$

where p and γ_c are the corresponding spectral index and cut-off Lorentz factor, respectively. This behaviour can be seen in Fig. 18, for instance, in the cases $k_B\overline{T}/mc^2 \approx 5.2 \times 10^{-2}$ and 3.5×10^{-1}. For the first temperature, we fitted equation (18) using $p \approx 2.2$ and $\gamma_c \approx 3.8$ (green dotted line), while for the second temperature we used $p \approx 1.9$ and $\gamma_c \approx 34$ (pink-dotted line). These fits were obtained using a maximum likelihood analysis considering only particles with energy larger than $10k_B\overline{T}$. The smallest particle energies considered in the fits are marked by the green and pink dots in Fig. 18. In Appendix A, we show that the spatial resolution that we are using ($\Delta = 0.35c/\omega_{p,0}$) is sufficient to capturing this non-thermal behaviour.

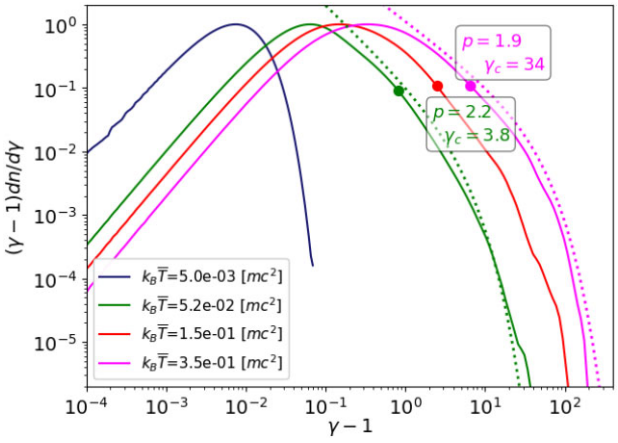

Figure 18. The evolution of the particle energy distribution for our fiducial run ST2D-20. Different colours represent different disc temperatures. The dotted lines correspond to fits to the non-thermal tails using equation (18), which use only particles with energies larger than 10 times the temperature for each spectrum. The solid dots in each spectrum mark the value of $\gamma - 1$ corresponding to that energy.

6.2 Role of $\omega_{c,0}/\Omega_0$

The role of the scale-separation ratio $\omega_{c,0}/\Omega_0$ is shown in Fig. 19, which shows the spectra of simulations with $\omega_{c,0}/\Omega_0 = 7$, 10, 14, 20, and 28, for temperatures $k_B\overline{T}/mc^2 = 5.2 \times 10^{-2}$ (panel a) and 3.5×10^{-1} (panel b). For each of these spectra, we show in dotted lines the corresponding fits using power laws with exponential cut-offs (equation 18). The dependencies of the fitted γ_c and p on $\omega_{c,0}/\Omega_0$ are shown in panels (a) and (b) of Fig. 20, respectively. By comparing with the black line in panel (a) ($\gamma_c = 36(\omega_{c,0}/\Omega_0)/20$), we see that for the spectra with temperature $k_B\overline{T}/mc^2 \approx 3.5 \times 10^{-1}$, γ_c behaves approximately as $\gamma_c \propto \omega_{c,0}/\Omega_0$. For $k_B\overline{T}/mc^2 \approx 5.2 \times 10^{-2}$, on the other hand, $\gamma_c \sim$ 4–10 with no clear dependence on $\omega_{c,0}/\Omega_0$.

This discrepancy in how γ_c depends on $\omega_{c,0}/\Omega_0$ is likely a manifestation of the underlying acceleration mechanism, which appears to be consistent with the expectation from reconnection driven acceleration. Indeed, the γ_c dependence on $\omega_{c,0}/\Omega_0$ for $k_B\overline{T}/mc^2 \approx 3.5 \times 10^{-1}$ is qualitatively consistent with the pair plasma magnetic reconnection results of Werner et al. (2016) in the limit of small system size, L. These results show power laws with supra-exponential cut-offs ($\mathrm{d}n/\mathrm{d}\gamma \propto \gamma^{-p} e^{-\gamma^2/\gamma_{c,\mathrm{rec}}^2}$) with $\gamma_{c,\mathrm{rec}} \approx 0.1L/\rho_0$, where $\rho_0 = mc^2/eB$ and B is the magnitude of the magnetic field in the upstream medium of the reconnecting plasmas. The corresponding value of L in our simulations can be estimated from the power spectrum of the x–z (poloidal) magnetic energy component, $\mathrm{d}(|B_x(k)|^2 + |B_z(k)|^2)/\mathrm{dln}\,(k)$, for runs with different scale-separation ratios shown in panel (a) of Fig. 4 (we use the poloidal magnetic field since this is the component that can experience reconnection in 2D). We see that the poloidal spectra peak at $k \sim \Omega_0/2\pi v_{A,0}$ fairly independent of the scale-separation ratio (as shown by Fig. 4a). Thus, a reasonable estimate for L is $L \sim 2\pi/k \sim (2\pi)^2 v_{A,0}/\Omega_0$. In addition,

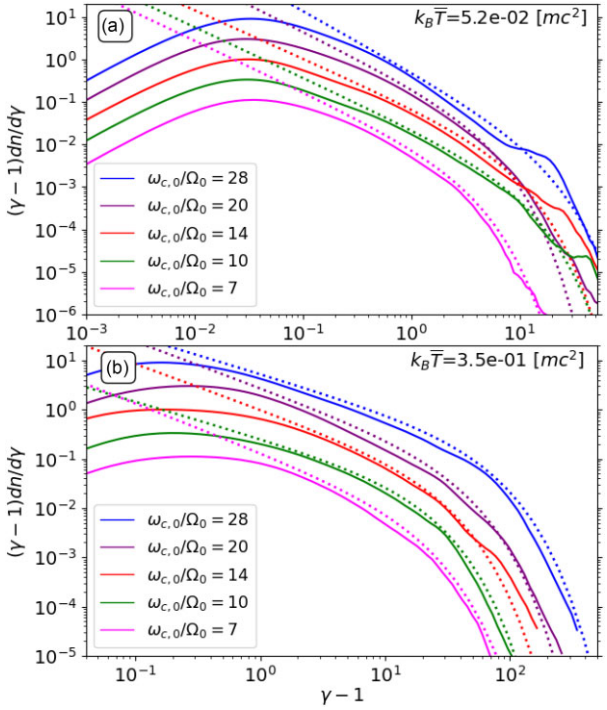

Figure 19. The particle spectra for runs with $\omega_{c,0}/\Omega_0 = 7$, 10, 14, 20, and 28, and with temperatures $k_B\overline{T}/mc^2 = 5.2 \times 10^{-2}$ (panel a) and 3.5×10^{-1} (panel b). For each spectra, we show in dotted lines a power-law fit with an exponential cut-off (as in equation 18). The normalizations of the spectra are arbitrary.

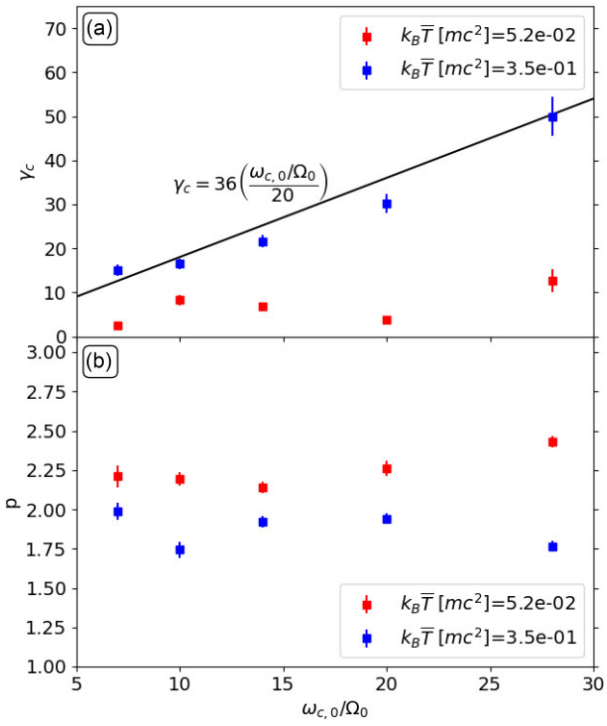

Figure 20. The values of γ_c and p obtained from fitting equation (18) to the obtained spectra as a function of $\omega_{c,0}/\Omega_0$. Different colours correspond to different disc temperatures.

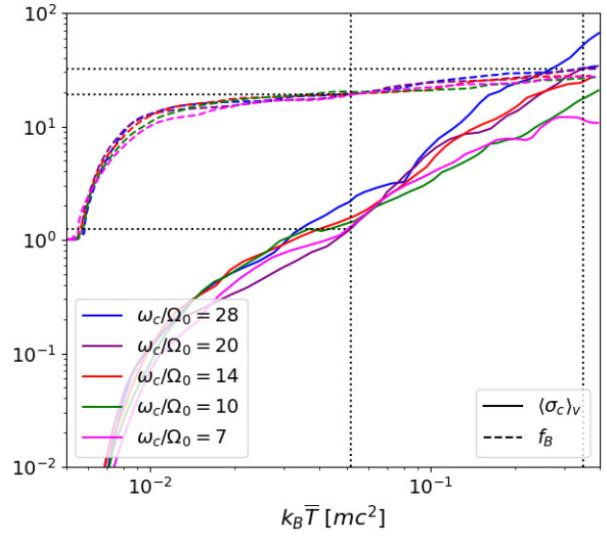

Figure 21. The values of $\langle\sigma_c\rangle_v$ and $f_B \equiv (\langle B^2\rangle_v)^{1/2}/B_0$ are shown in solid and dashed lines as a function of $\overline{T}$ and for simulations with $\omega_{c,0}/\Omega_0 = 7$, 10, 14, 20, and 28.

we can estimate $\rho_0 = mc^2/eB \approx c/(\omega_{c,0}f_B)$, where f_B ($\equiv (\langle B^2\rangle_v)^{1/2}/B_0$) is the root mean square amplification factor of the magnetic field in the disc at a given time. Thus, if reconnection is the main driver of particle acceleration in our runs, γ_c should be close to $\gamma_{c,\mathrm{rec}}$, which would be given by

$$\gamma_{c,\mathrm{rec}} \approx 0.1\frac{L}{\rho_0} \approx 36\left(\frac{\omega_{c,0}/\Omega_0}{20}\right)\left(\frac{f_B}{30}\right), \tag{19}$$

where we have used that $v_{A,0}/c = 10^{-2}$ in all our simulations. The value f_B as a function of $\overline{T}$ is shown in dashed lines in Fig. 21 for different values of $\omega_{c,0}/\Omega_0$. We see that when $k_B\overline{T}/mc^2 \approx 3.5 \times 10^{-1}$, $f_B \approx 30$, fairly regardless of the scale-separation ratio. This means that the expected $\gamma_{c,\mathrm{rec}}$ at $k_B\overline{T}/mc^2 = 3.5 \times 10^{-1}$ is

$$\gamma_{c,\mathrm{rec}} \approx 36\left(\frac{\omega_{c,0}/\Omega_0}{20}\right). \tag{20}$$

The black line in panel (a) of Fig. 20 shows the case $\gamma_c = \gamma_{c,\mathrm{rec}}$, where $\gamma_{c,\mathrm{rec}}$ is given by equation (20). We see that $\gamma_{c,\mathrm{rec}}$ reproduces well the behaviour of γ_c in our runs with $k_B\overline{T}/mc^2 = 3.5 \times 10^{-1}$.

The behaviour $\gamma_{c,\mathrm{rec}} \approx 0.1L/\rho_0$ expected from reconnection is valid as long as $L/\sigma_c^u\rho_0 \lesssim 40$ (Werner et al. 2016), where σ_c^u corresponds to the cold sigma parameter in the upstream medium of the reconnection simulations. We estimate σ_c^u using $\langle\sigma_c\rangle_v$ in our runs when $k_B\overline{T}/mc^2 = 3.5 \times 10^{-1}$, which is $\langle\sigma_c\rangle_v \sim$ 10–50 for the range of $\omega_{c,0}/\Omega_0$ considered, as shown by the solid lines in Fig. 21.[4] Thus, using equation (19), we obtain that

$$\frac{L}{\rho_0\sigma_c} \sim 18\left(\frac{\omega_{c,0}/\Omega_0}{20}\right)\left(\frac{f_B}{30}\right)\left(\frac{\langle\sigma_c\rangle_v}{20}\right)^{-1}. \tag{21}$$

Equation (21) thus implies that all of our simulations satisfy the restriction $L/\rho_0\sigma_c \lesssim 40$ when $k_B\overline{T}/mc^2 = 3.5 \times 10^{-1}$, even in our run with the largest scale-separation ratio, $\omega_{c,0}/\Omega_0 = 28$. Interestingly, Fig. 21 also shows that, when $k_B\overline{T}/mc^2 = 5.2 \times 10^{-2}$,

[4]Since we want to estimate the equivalent of the upstream cold sigma parameter σ_c^u, we are mainly interested in the values of σ_c outside the current sheets, where σ_c is the largest. Thus, given that in our runs $\langle\sigma_c\rangle_v$ ($= \langle B^2/4\pi nm^2\rangle_v$) $> \overline{\sigma}_c$ ($=\langle B^2\rangle_v/4\pi\langle n\rangle_v m^2$), we are using $\langle\sigma_c\rangle_v$ instead of $\overline{\sigma}_c$ as our estimate of σ_c^u.

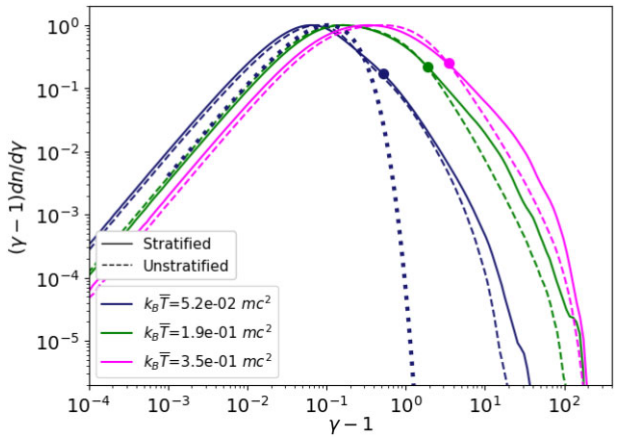

Figure 22. Particle energy distribution for stratified (solid) and unstratified (dashed) runs with the same magnetization $\omega_c/\Omega_0 = 20$ (runs ST2D-20 and UN2D-20, respectively). Different colours represent different temperatures. The dotted line corresponds to a Maxwell–Boltzmann spectrum. In order to help the visual distinction between the thermal and non-thermal parts of the spectra, the solid dots mark the value of $\gamma - 1$ corresponding to an energy of $10k_B\overline{T}$.

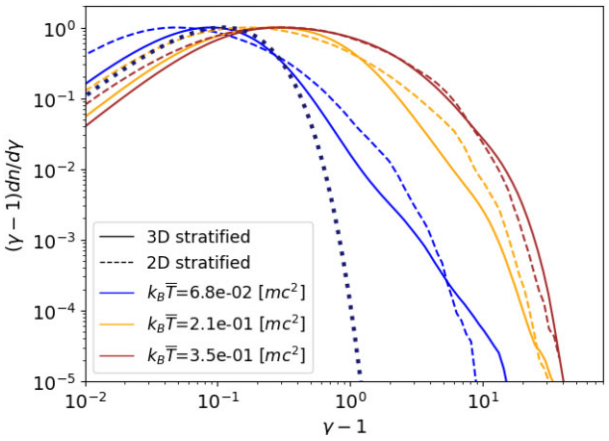

Figure 23. Spectra from simulations in 2D (dashed) and 3D (solid), both with a scale-separation ratio $\omega_{c,0}/\Omega_0 = 3.5$ (runs ST2D-3.5 and ST3D-3.5., respectively). The different colours represent temperatures.

$\langle\sigma_c\rangle_v \sim 1$, and $f_B \approx 20$, implying that for that temperature $L/\rho_0\sigma_c \sim 240(\omega_{c,0}/\Omega_0)/20 \gtrsim 40$. This means that, if particle acceleration is driven by magnetic reconnection at $k_B\overline{T}/mc^2 = 5.2\times10^{-2}$, γ_c should not be proportional to $\omega_{c,0}/\Omega_0$. Instead, a weaker dependence on L is expected for 2D runs, since in that case γ_c likely grows more slowly with time as $\gamma_c \propto t^{1/2}$ (Petropoulou & Sironi 2018; Hakobyan et al. 2021). This possibly explains why we do not observe a clear dependence of γ_c on $\omega_{c,0}/\Omega_0$ in the case of $k_B\overline{T}/mc^2 = 5.2\times10^{-2}$.

The values of p for $k_B\overline{T}/mc^2 = 5.2\times10^{-2}$ and 3.5×10^{-1} seen in panel (b) of Fig. 20 are close to $p\sim2.2$ and $\sim$1.9, respectively, and do not show a clear dependence on the scale-separation ratio. This is also consistent with acceleration being driven by reconnection. For instance, for $L/\rho_0\sigma_c \gtrsim 40$ and $\sigma_c = 3$ (a case close to our results with $k_B\overline{T}/mc^2 = 5.2\times10^{-2}$, where $\langle\sigma_c\rangle_v \sim$ 1–2; see Fig. 21), Werner et al. (2016) predict $p\sim$ 2.3–2.5. Whereas for $L/\rho_0\sigma_c \lesssim 40$ and $\sigma_c =$ 10–30 (close to our results with $k_B\overline{T}/mc^2 = 3.5\times10^{-1}$, where $\langle\sigma_c\rangle_v \sim$ 10–50; see Fig. 21), the results of Werner et al. (2016) show $p\sim$ 1.4–1.9.

6.3 Effect of stratification on the acceleration

The previous discussion underscores the importance of plasma conditions, in particular σ_c and f_B, in determining the efficiency of non-thermal particle acceleration. Since these conditions vary significantly between stratified and unstratified simulations (as shown by Fig. 6), we expect the acceleration efficiency in these two types of runs to be different. Fig. 22 compares spectra from run ST2D-20 with the equivalent spectra in the unstratified run UN2D-20 at the same values of $\overline{T}$. We see that the spectra in the unstratified run are always softer than in the stratified run ST2D-20. This is consistent with the fact that, for a given temperature, in run UN2D-20 the value of $\overline{\sigma}_c$ is smaller than in the run ST2D-20 (as seen in panel c of Fig. 6), which favours softer non-thermal acceleration in the unstratified case.

6.4 Acceleration in 2D versus 3D

In Fig. 23, we compare spectra from the 2D and 3D simulations ST2D-3.5 and ST3D-3.5, both with a scale-separation ratio $\omega_{c,0}/\Omega_0 = 3.5$, for $k_B\overline{T}/mc^2 = 6.8\times10^{-2}$, 2.1×10^{-1}, and 3.5×10^{-1}. As expected from our previous discussion on the dependence of γ_c on $\omega_{c,0}/\Omega_0$, the 2D run ST2D-3.5 should produce a non-thermal tail of rather short extension, which is what we see in Fig. 23. However, it is still interesting to verify whether its main features are reproduced in the 3D run ST3D-3.5. We see that, although the spectra show somewhat different shapes, they both feature non-thermal tails with similar maximum energies. In particular, when $k_B\overline{T}/mc^2 = 3.5\times10^{-1}$, the 2D and 3D spectra look very similar, suggesting that, at least for small-scale separations, 3D effects maintain the main particle accelerating properties of the MRI turbulence observed in 2D. However, 3D simulations with larger scale separation appear necessary to check whether in 3D runs γ_c follows the same dependency on scale separation shown for 2D in Figs 19 and 20. This is particularly interesting given recent results showing that 3D reconnection may allow significantly larger values of γ_c (Zhang, Sironi & Giannios 2021; Zhang et al. 2023).

Even though the non-thermal particle behaviour in our runs suggests a significant role of magnetic reconnection in the acceleration of particles, our simulations may be subject to effects that are not present in previous magnetic reconnection studies. These include particle escape from the disc, stochastic acceleration by the MRI turbulence (e.g. Kimura, Tomida & Murase 2019; Sun & Bai 2021), and the action of various kinetic instabilities that may contribute to field dissipation and/or particle acceleration, including, for example, the drift kink instability (Zenitani & Hoshino 2007) and the ion-cyclotron instability (Ley et al. 2019). We thus defer to future research a detailed determination of the dominant acceleration process(es) as well as the role of the scale-separation ratio by including 2D and 3D runs with larger values of $\omega_{c,0}/\Omega_0$.

7 VALIDATION OF ASSUMPTIONS

In this section, we use our obtained MRI turbulence behaviour to validate the assumptions underlying the shearing coordinates method used in this work, which is described in Section 2.2.

The fact that the peaks of the poloidal and toroidal spectra of $\mathbf{B}^T$ are close to $k\,2\pi\,v_{A,0}/\,\Omega_0 \sim 1$ in 2D and 3D (as shown in Section 4.1) is important for the validation of the shearing coordinates approach. Indeed, since $\mathbf{B}^D$ only depends on t and z, subtracting this quantity from the total field does not change the power spectra of the magnetic

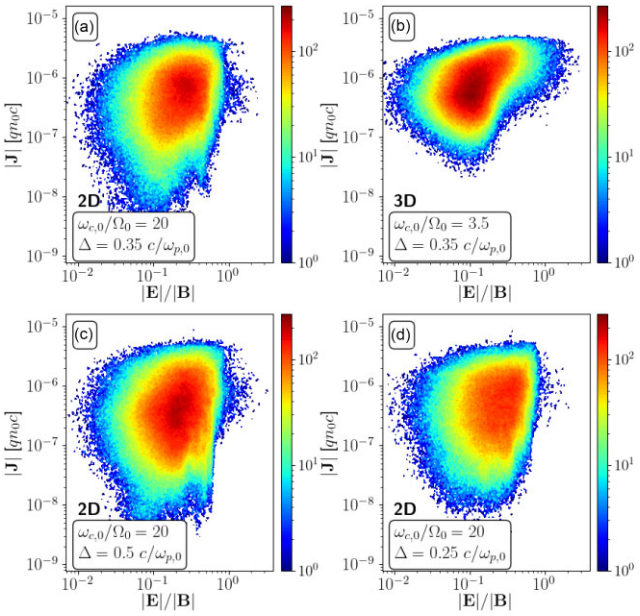

Figure 24. Panels (a) and (b) show the distribution of current density magnitude $|\mathbf{J}|$ and the $|\mathbf{E}|/|\mathbf{B}|$ ratio in the stratified run ST2D-20 and ST3D-3.5 at time $t = 5\ [2\pi/\Omega_0]$, respectively. Panels (c) and (d) show the same for simulations ST2D-20LR and ST2D-20HR, which are analogous to run ST2D-20 but using lower and higher spatial resolutions ($\Delta = 0.5$ and 0.25 $[c/\omega_{p,0}]$, respectively).

field for k_x and k_y ($k_x = \hat{x}\cdot\mathbf{k}$ and $k_y = \hat{y}\cdot\mathbf{k}$, where $\mathbf{k}$ is the wave vector in Fourier space). Thus, the dominance of $k\,2\pi\,v_{A,0}/\,\Omega_0 \sim 1$ for poloidal and toroidal components of $\mathbf{B}^T$ implies that the dominant wavelength of the magnetic fluctuations along the x and y axis is given by $\sim 2\pi\,v_{A,0}/\Omega_0$. This is indeed one of the assumptions made in our implementation of the shearing coordinates approach (Section 2.2), which, combined with the condition $v_{A,0}/c \ll 1$, allowed us to drop the y-dependent terms in the field evolution equations (4) and (5), as well as to obtain the momentum and particle position evolution equations (12) and (13).

Our shearing coordinates approach also assumes that the electric field in the MRI turbulence is either smaller or of the same order of the magnetic field ($|\mathbf{E}|/|\mathbf{B}| \lesssim 1$). To support this assumption, panels (a) and (b) of Fig. 24 show an example of the distribution of the electric current magnitude $|\mathbf{J}|$ and the $|\mathbf{E}|/|\mathbf{B}|$ ratio for runs ST2D-20 and ST3D-3.5 at time $t = 5\ [2\pi/\Omega_0]$. We see that in both cases the entire distribution satisfies $|\mathbf{E}|/|\mathbf{B}| \lesssim 3$, including the regions with the largest value of $|\mathbf{J}|$, which are expected to correspond to reconnecting current sheets. In order to show that this behaviour is not affected by the spatial resolution of our simulations, panels (c) and (d) show the same results as panel (a), but for runs ST2D-20LR and ST2D-20HR of Table 1, which are analogous to run ST2D-20 but with lower and higher spatial resolutions, respectively ($\Delta = 0.5$ and 0.25 $[c/\omega_{p,0}]$, respectively). We see that the highest resolution case reaches even smaller values of $|\mathbf{E}|/|\mathbf{B}|$, and shows a clearer trend in which the locations with the largest $|\mathbf{E}|/|\mathbf{B}|$ tend to have the largest $|\mathbf{J}|$.

Finally, another important assumption in our simulations is that $\boldsymbol{J} \approx c\nabla\times\boldsymbol{B}/4\pi$, valid in the non-relativistic MHD regime. This assumption implies that the cold sigma parameter σ_c (equivalent to the square of the instantaneous ratio v_A/c) must be on average significantly smaller than unity. In our stratified setup, this condition is necessarily broken at sufficiently large values of $|z|$, due to the significant drop in plasma density outside of the disc. Also,

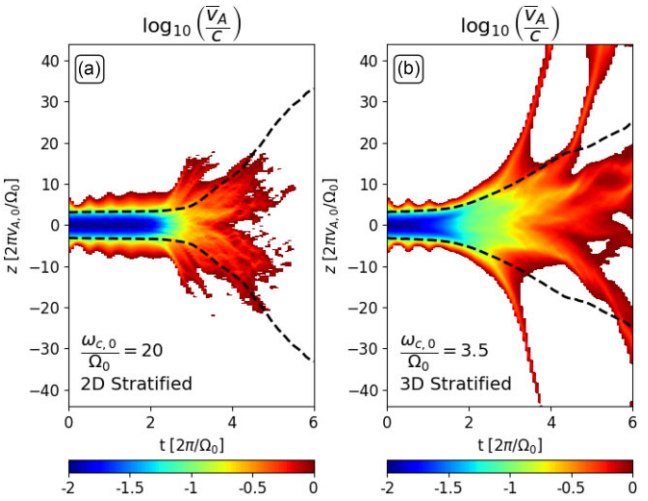

Figure 25. Panel (a) shows $\overline{v}_A/c$ for the 2D run ST2D-20, where $\overline{v}_A/c = (\langle B^2\rangle_x/4\pi\,\langle n\rangle_x mc^2)^{1/2}$. Panel (b) shows the same as panel (a), but for the 3D run ST3D-3.5. In this case, $\overline{v}_A/c = (\langle B^2\rangle_{x-y}/4\pi\,\langle n\rangle_{x-y} mc^2)^{1/2}$. The dashed line shows the scale height of the disc, defined by $|z| = H(\overline{T})$.

Fig. 7(b) shows that, for $t \gtrsim 5[2\pi/\Omega_0]$, $\overline{\sigma}_c$ (defined within the disc) becomes $\gtrsim 1$, implying that our results are strictly valid only until $t \sim 5[2\pi/\Omega_0]$. These restrictions are verified in Fig. 25, which shows an average of the Alfvén velocity in our 2D and 3D runs ST2D-20 and ST3D-3.5 (panels a and b, respectively), as a function t and z. In this case, the average Alfvén velocity is defined as

$$\frac{\overline{v}_A}{c} \equiv \begin{cases} \left(\frac{\langle B^2\rangle_x}{4\pi\,\langle n\rangle_x mc^2}\right)^{1/2} & \text{for run ST2D-20 and} \\ \left(\frac{\langle B^2\rangle_{x-y}}{4\pi\,\langle n\rangle_{x-y} mc^2}\right)^{1/2} & \text{for run ST3D-3.5.} \end{cases} \tag{22}$$

We see that, for run ST2D-20, the disc region (defined by $|z| < H(\overline{T})$ and delimited by the dashed lines) satisfies $\overline{v}_A/c \lesssim 1$ only until $t \sim 5[2\pi/\Omega_0]$. For run ST3D-3.5, $\overline{v}_A/c \lesssim 1$ is satisfied across most of the disc volume until $t \sim 6[2\pi/\Omega_0]$. These considerations reinforce the idea that our results are strictly valid only in the sub-relativistic regime ($k_B\overline{T}/mc^2 \lesssim 0.3$), which, according to Fig. 7(b), occurs at $t \lesssim 5[2\pi/\Omega_0]$.

Given that our treatment is only valid in the subrelativistic regime, our particle acceleration results have been presented only until $k_B\overline{T}/mc^2 \sim 0.3$. Notice, however, that the particle acceleration properties at $k_B\overline{T}/mc^2 \sim 0.3$ are consistent with them being determined by the 'upstream' cold sigma parameter, σ_c^u, which correspond to the cold sigma outside of the current sheets (as explained in Section 6.2). This σ_c^u is expected to be relatively large, because of the low plasma density and high magnetic field in the regions outside of the reconnection current sheets. As discussed in footnote 4, we estimated σ_c^u using $\langle\sigma_c\rangle_v$, which reaches $\langle\sigma_c\rangle_v \sim 20$ when $k_B\overline{T}/mc^2 \sim 0.3$ (see Fig. 21). Thus, even though by $k_B\overline{T}/mc^2 \sim 0.3$ the plasma in the disc is approximately still within the subrelativistic regime, the upstream regions of the reconnecting plasma appear to be (locally) in a fairly relativistic state. This is consistent with the fact that the obtained cut-off Lorentz factor γ_c and spectral indices of the non-thermal particles at $k_B\overline{T}/mc^2 \sim 0.3$ follow quite well the expectations from the relativistic reconnection study of Werner et al. (2016).

8 CONCLUSIONS

In this work, we have studied the effect of stratification on the collisionless MRI using 2D and 3D PIC simulations. Comparing 2D stratified and unstratified runs, we found that stratification affects the evolution of the disc conditions, due to the presence of outflows and disc expansion, leading to a decrease in the amplification of magnetic field energy density in the turbulent non-linear MRI regime. However, the expansion of the disc also decreases the plasma pressure and density, resulting in a highly magnetized disc, with smaller β and larger cold magnetization parameter σ_c compared to the unstratified case. Indeed, in the non-linear regime the disc is magnetic-pressure supported with $\beta \sim 0.4$, which is a factor $\sim$5 smaller than the value reached by its unstratified counterpart. In the disc region, our runs also give rise to a significant large scale and predominantly toroidal dynamo-like field $\mathbf{B}^D$ ($\equiv \langle \mathbf{B} \rangle_x$ in 2D), whose dominant scale length follows the disc scale height. Although a large-scale $\langle \mathbf{B} \rangle_x$ field also appears in the 2D unstratified case, its scale length is $\sim$4 times smaller. The increased magnetization of our 2D stratified runs produces an effective viscosity α in the disc that reaches $\alpha \sim 1$, which is a factor $\sim$5 larger than in the equivalent unstratified case. This viscosity is dominated by the Maxwell stress, α_M, with a small contribution of the anisotropic stress, α_A. This small α_A is consistent with the regulation of pressure anisotropies by kinetic microinstabilities in the low β regime.

Even though our 2D and 3D stratified simulations produce similar results, some differences are present. In order to assess them, we compared 2D and 3D runs focusing on a specific case with small-scale separation, $\omega_{c,0}/\Omega_0 = 3.5$. In the early phase of the non-linear MRI stage (i.e. $\sim$1–2 orbits after the triggering of the instability), 3D simulations exhibit a significantly lower amplification of the magnetic field energy density compared to their 2D counterpart. This is consistent with the fact that 3D runs allow reconnection of the toroidal component of the magnetic field (as shown in the recent work of Bacchini et al. 2022), which is impossible in 2D. This primarily affects the effective viscosity α and the plasma β, which are, respectively, $\sim$3–4 times smaller and larger in the 3D case. However, after this initial stage (at $t \sim 4\ [2\pi/\Omega_0]$), our 2D and 3D simulations are more similar, with β reaching essentially the same values and the effective viscosity α being only $\sim$2 times smaller in 3D (in 3D, $\alpha \approx 0.5$ during the whole non-linear MRI stage). This transition at $t \sim 4\ [2\pi/\Omega_0]$ occurs because of the growing importance of the large-scale dynamo-like field $\mathbf{B}^D$ ($\equiv \langle \mathbf{B} \rangle_{x-y}$ in 3D). Indeed, after an initial stage in which the turbulent field $\mathbf{B}^T$ ($=\mathbf{B} - \mathbf{B}^D$) dominates, the dynamo-like field becomes larger than the turbulent field in the 3D runs, while in 2D it reaches values comparable to the turbulent field. Since the dynamo field has almost the same amplitude in 2D and 3D, the total fields in these two types of runs differ by a small amount after $t \sim 4\ [2\pi/\Omega_0]$. Also, in this dynamo-dominated period, the 3D viscosity is mainly produced by the dynamo-like field, while in 2D the turbulent and dynamo fields contribute comparably to α. In 3D the disc viscosity is also dominated by the Maxwell stress, α_M, with a small contribution from the anisotropic stress, α_A. This is also consistent with the action of pressure anisotropy-driven kinetic microinstabilities in the 3D case, as it occurs in 2D. Our 2D and 3D results in terms of α, β, and dynamo-like field behaviours are reasonably consistent with previous 3D MHD simulations of stratified discs with similar initial conditions (e.g. Bai & Stone 2013; Salvesen et al. 2016).

In terms of particle acceleration, in our 2D runs we find that the particle spectra in the non-linear MRI stage follow power laws with exponential cut-offs, with power-law indices $p \approx 2.2$–1.9 for disc temperatures $\sim 0.05 - 0.3\, mc^2$. Additionally, depending on the value of σ_c during the non-linear MRI stage, the maximum energy attained by the particles is either proportional to the scale separation $\omega_{c,0}/\Omega_0$ or fairly independent of this parameter, which appears to be consistent with previous magnetic reconnection studies (Werner et al. 2016). Particle acceleration in our 2D unstratified runs appears to be less efficient than in the analogous stratified case. This is likely due to the smaller cold magnetization parameter σ_c attained in the unstratified simulations. Furthermore, the particle acceleration observed in our 2D run with $\omega_{c,0}/\Omega_0 = 3.5$ is well reproduced by its analogous 3D simulation, suggesting that 3D effects should maintain most of the acceleration properties of the MRI turbulence. However, 3D runs with larger scale-separation ratio are needed to confirm this trend.

In summary, our results suggest that including disc stratification in shearing-box PIC simulations of the MRI is important for studying its saturation, effective viscosity generation, and particle acceleration physics. Interestingly, 2D and 3D simulations give quite similar results for the scale-separation ratios used in this work, especially after the magnetic field energy becomes dominated by a large-scale, dynamo-like field (which occurs $\sim$1–2 orbits after the triggering of the instability). However, recent PIC simulation studies show that the maximum energies attained by particles accelerated by reconnection may be significantly higher in 3D (Zhang et al. 2021, 2023). Since our particle acceleration results appear consistent with reconnection, we expect these differences to be apparent in future 2D and 3D simulations with large enough scale separation. We also note that our results refer to a specific case of initial plasma conditions. Further research is thus needed to clarify the effects of changing the initial β and/or temperature in the disc, potentially leading to a more distinct differentiation between an unmagnetized disc and a magnetized corona (e.g. Salvesen et al. 2016). Finally, obtaining emission predictions from our stratified setup requires including the effect of realistic mass ratios on the dynamic and thermodynamic properties of the MRI turbulence, as well as incorporating the effect of electron cooling, which may modify the overall disc dynamics and affect the emission spectrum (Sridhar, Sironi & Beloborodov 2023). We defer these important aspects of the collisionless MRI problem to future work.

ACKNOWLEDGEMENTS

Astor Sandoval acknowledges support from the Center for Excellence in Astrophysics and Associated Technologies (CATA) through ANID, BASAL, FB210003. M. Riquelme thanks support from a Fondecyt Regular grant no. 1191673 and from CONICYT/Quimal 190011. Anatoly Spitkovsky acknowledges the support of NSF grants PHY-2206607 and AST-1814708. F. Bacchini acknowledges support from the FED-tWIN programme (profile Prf-2020-004, project 'ENERGY') issued by BELSPO, and from the FWO Junior Research Project G020224N granted by the Research Foundation – Flanders (FWO). The computational resources and services used in this work were provided by the National Laboratory for High Performance Computing (NLHPC) of the Center for Mathematical Modeling of University of Chile (ECM-02) and the VSC (Flemish Supercomputer Center), funded by the Research Foundation – Flanders (FWO) and the Flemish Government – department EWI.

DATA AVAILABILITY

The data underlying this article will be shared on reasonable request to the corresponding author.

REFERENCES

Bacchini F., Arzamasskiy L., Zhdankin V., Werner G. R., Begelman M. C., Uzdensky D. A., 2022, ApJ, 938, 86
Bai X.-N., Stone J. M., 2013, ApJ, 767, 30
Balbus S. A., Hawley J. F., 1991, ApJ, 376, 214
Balbus S. A., Hawley J. F., 1998, Rev. Mod. Phys., 70, 1
Belyaev M. A., 2015, New Astron., 36, 37
Buneman O., 1993, Computer Space Plasma Physics. Terra Scientific, Tokyo
Cerutti B., Philippov A., Parfrey K., Spitkovsky A., 2015, MNRAS, 448, 606
Esin A. A., McClintock J. E., Narayan R., 1997, ApJ, 489, 865
Guilet J., Ogilvie G., 2012, MNRAS, 424, 2097
Hakobyan H., Petropoulou M., Spitkovsky A., Sironi L., 2021, ApJ, 912, 48
Hawley J. F., Gammie C. F., Balbus S. A., 1995, ApJ, 440, 742
Hellinger P., Trávníček P., Kasper J. C., Lazarus A. J., 2006, Geophys. Res. Lett., 33, L09101
Hirabayashi K., Hoshino M., 2017, ApJ, 842, 36
Hoshino M., 2013, ApJ, 773, 118
Hoshino M., 2015, Phys. Rev. Lett., 114, 061101
Inchingolo G., Grismayer T., Loureiro N. F., Fonseca R. A., Silva L. O., 2018, ApJ, 859, 149
Jacquemin-Ide J., Lesur G., Ferreira J., 2021, A&A, 647, A192
Kimura S., Tomida K., Murase K., 2019, MNRAS, 485, 163
Kunz M. W., Stone J. M., Quataert E., 2016, Phys. Rev. Lett., 117, 235101
Ley F., Riquelme M., Sironi L., Verscharen D., Sandoval A., 2019, ApJ, 880, 100
Ley F., Zweibel E., Riquelme M., Sironi L., Miller D., Tran A., 2023, ApJ, 947, 89
Passot T., Sulem P. L., 2015, ApJ, 812, L37
Petropoulou M., Sironi L., 2018, MNRAS, 481, 5687
Riquelme M. A., Quataert E., Sharma P., Spitkovsky A., 2012, ApJ, 755, 50
Riquelme M. A., Quataert E., Verscharen D., 2015, ApJ, 800, 27
Rothstein D., Lovelace R., 2008, ApJ, 677, 1221
Salvesen G., Simon J. B., Armitage P. J., Begelman M. C., 2016, MNRAS, 457, 857
Schiff L. I., 1939, Proc. Natl Acad. Sci., 25, 391
Shakura N. I., Sunyaev R. A., 1973, A&A, 24, 337
Sharma P., Hammett G., Quataert E., Stone L., 2006, ApJ, 637, 952
Sharma P., Quataert E., Hammett G., Stone L., 2007, ApJ, 667, 714
Sironi L., Cerutti B., 2017, in Torres D., ed., Astrophysics and Space Science Library, Vol. 446, Modelling Pulsar Wind Nebulae. Springer, Cham
Sironi L., Giannios D., Petropoulou M., 2016, MNRAS, 462, 48
Spitkovsky A., 2005, in Bulik T., Rudak B., Madejski G., eds, AIP Conf. Proc. 801, Astrophysical Sources of High Energy Particles and Radiation. AIP, Melville, NY, p. 345
Sridhar N., Sironi L., Beloborodov A., 2023, MNRAS, 518, 1301
Sun X., Bai X.-N., 2021, MNRAS, 506, 1128
Walker J., Lesur G., Boldyrev S., 2016, MNRAS, 457, L39
Werner G. R., Uzdensky D. A., Cerutti B., Nalewajko K., Begelman M. C., 2016, ApJ, 816, L8
Yoon D., Chatterjee K., Markoff S. B., van Eijnatten D., Younsi Z., Liska M., Tchekhovskoy A., 2020, MNRAS, 499, 3178
Yuan F., Narayan R., 2014, ARA&A, 52, 529
Zenitani S., Hoshino M., 2007, ApJ, 670, 702
Zhang H., Sironi L., Giannios D., 2021, ApJ, 922, 261
Zhang H., Sironi L., Giannios D., Petropoulou M., 2023, ApJ, 956, L36

APPENDIX A: SPATIAL RESOLUTION CONVERGENCE

In this appendix, we performed numerical convergence tests for our fiducial simulation ST2D-20, by comparing our results for different spatial resolutions. Table 1 shows the parameters of simulations with different values of $\Delta[c/\omega_{p,0}]$, including our fiducial case (ST2D-20, $\Delta[c/\omega_{p,0}] = 0.35$), an equivalent low resolution (ST2D-20LR, $\Delta[c/\omega_{p,0}] = 0.5$), and a high resolution (ST2D-20HR, $\Delta[c/\omega_{p,0}] = 0.25$) simulations. All the other parameters are essentially the same between these three runs. Panels (a) and (b) of Fig. A1 show $\langle B^2\rangle_v$, $\overline{\beta}$, $\overline{\sigma}_c$, and $\overline{T}$ for these runs, with the starting time of each simulation slightly shifted to make their exponential MRI growth phases coincide. The two highest resolution runs, ST2D-20 and ST2D-20HR, behave in almost indistinguishable manners, while the case with the lowest resolution (ST2D-20LR) shows a small increase in $\langle B^2\rangle_v$, $\overline{\sigma}_c$, and $\overline{T}$. The similarity between the two highest resolution runs implies that the spatial resolution used in our fiducial run ST2D-20 is large enough to capture the overall evolution of the magnetic field and plasma temperature in the disc.

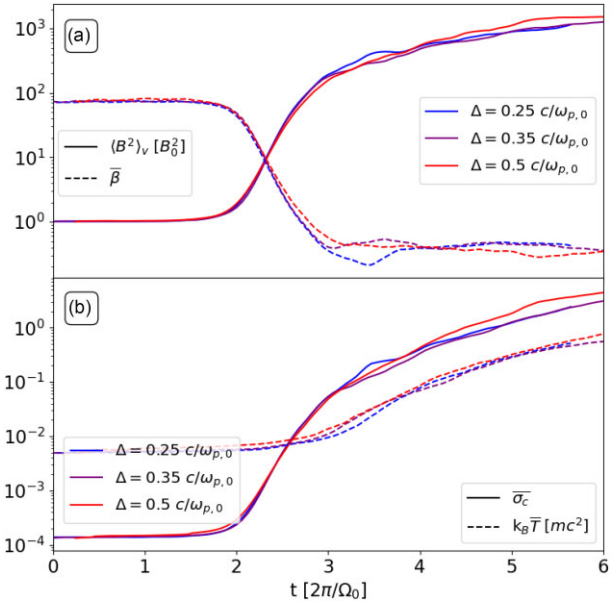

Figure A1. Same as Fig. 7, but for different spatial resolutions at fixed $\omega_{c,0}/\Omega_0 = 20$.

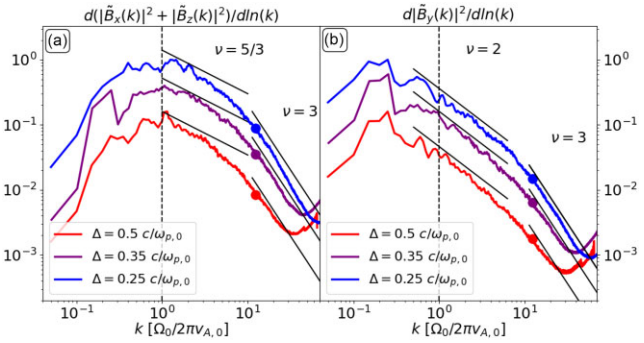

Figure A2. Same as panels (a) and (b) of Fig. 4, but for different spatial resolutions at fixed $\omega_{c,0}/\Omega_0 = 20$.

Fig. A2 shows the poloidal and toroidal (panels a and b, respectively) power spectra of the magnetic turbulence for these three runs at $k_B T \approx 0.3$ [mc^2]. It can be seen that the poloidal and toroidal parts of the turbulence are essentially unaffected by the resolution. The only difference occurs, at sub-Larmor scales ($k\rho_l \gtrsim 1$; $k\rho_l = 1$ corresponds to the solid dots in both panels), where the spectra get interrupted by noise at progressively smaller values of k as the resolution decreases. Although these differences in resolution may in principle have an impact on particle acceleration, especially if the current sheets are not well resolved, we verified that the particle

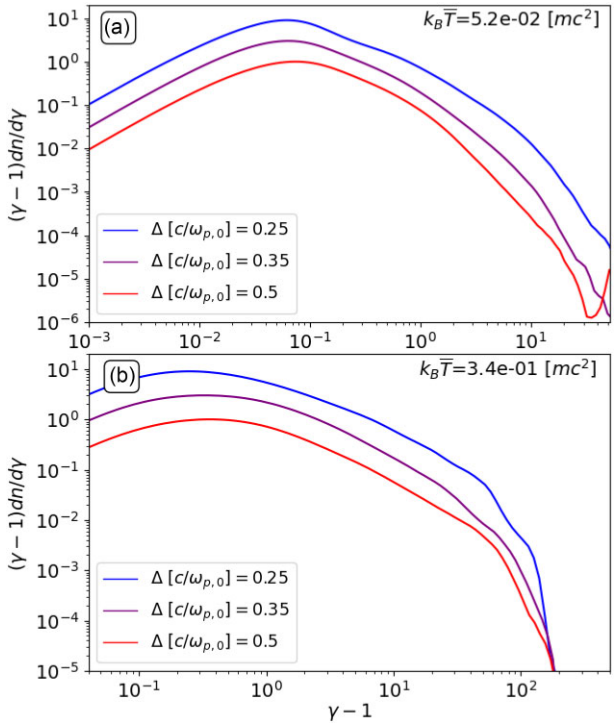

Figure A3. Same as Fig. 19, but for different spatial resolutions at fixed $\omega_{c,0}/\Omega_0 = 20$.

spectra do not change significantly for the three values of $\Delta[c/\omega_{p,0}]$. Indeed, Fig. A3 shows the spectra of the same runs ST2D-20, ST2D-20LR, and ST2D-20HR for the same two temperatures shown in Fig 19. Apart from a slight hardening of the spectra as the resolution increases, no significant differences are observed, especially between the two highest resolution runs.

This paper has been typeset from a TEX/LATEX file prepared by the author.